npj | Quantum Materials

www.nature.com/npjquantmats

ARTICLE OPEN

Check for updates

Quantum oscillations from networked topological interfaces in a Weyl semimetal

I-Lin Liu[1,2,3]✉, Colin Heikes[1,4], Taner Yildirim[1], Chris Eckberg[2], Tristin Metz[2], Hyunsoo Kim[2], Sheng Ran[1,2,3,5], William D. Ratcliff[1], Johnpierre Paglione[2] and Nicholas P. Butch[1,2]✉

Layered transition metal chalcogenides are promising hosts of electronic Weyl nodes and topological superconductivity. $MoTe_2$ is a striking example that harbors both noncentrosymmetric T_d and centrosymmetric T′ phases, both of which have been identified as topologically nontrivial. Applied pressure tunes the structural transition separating these phases to zero temperature, stabilizing a mixed T_d–T′ matrix that entails a network of interfaces between the two nontrivial topological phases. Here, we show that this critical pressure range is characterized by distinct coherent quantum oscillations, indicating that the difference in topology between topologically nonvtrivial T_d and T′ phases gives rise to an emergent electronic structure: a network of topological interfaces. A rare combination of topologically nontrivial electronic structures and locked-in transformation barriers leads to this counterintuitive situation, wherein quantum oscillations can be observed in a structurally inhomogeneous material. These results further open the possibility of stabilizing multiple topological phases coexisting with superconductivity.

npj Quantum Materials (2020)5:62 ; https://doi.org/10.1038/s41535-020-00264-8

INTRODUCTION

Topologically protected electronic states at material interfaces are attractive because they cannot be destroyed by many types of perturbations[1,2]. An especially fruitful host of such exotic states is $MoTe_2$, which has had both its bulk orthorhombic T_d phase, and hole-doped monolayer specimens identified as possible topological superconductors[3–5]. In addition, a topological superconducting phase was recently discovered in sulfur-substituted samples, with S_{+-}-wave pairing[6]. $MoTe_2$ also features topologically nontrivial normal states: the T_d phase has been identified as a type II Weyl semimetal[7–10], whereas the monoclinic T′ phase is predicted to be a higher-order topological material[11]; the latter is also found to describe the T_d phase in some calculations[11]. In this work, we demonstrate via quantum oscillations and neutron scattering measurements, and first-principles calculations, how pressure drives $MoTe_2$ between the T_d and T′ phases, through an intermediate mixed-phase region. The mixed-phase region gives rise to a network of topological interface states that yield quantum oscillations that survive despite the strong structural disorder.

RESULTS

Orthorhombic T_d–$MoTe_2$

The first-order structural transition separating the T′ and T_d phases in $MoTe_2$ has a distinct pressure dependence (Fig. 1a). At ambient pressure, the inversion-symmetric T′ phase is stable at room temperature, only transforming into the noncentrosymmetric T_d phase when cooled below roughly 250 K[3,12]. Neutron diffraction allows the determination of the relative volume fraction of these phases under different conditions[12]. As pressure increases, the transition temperature decreases. At pressures higher than 0.8 GPa, a completely different phenomenon emerges, where a roughly balanced mixture of the T′ and T_d phases stabilizes over an appreciable temperature range, and crucially, extends to the lowest measured temperatures. The existence of this frozen mixed-phase region is stabilized by the lack of sufficient entropy at these suppressed temperatures for atoms to move to their lowest-energy configuration, implying that there is a dominant extrinsic transformation energy barrier between two energetically nearly degenerate structures[12].

The basic components underlying the Weyl semimetallic state of the low-pressure, low-temperature T_d phase are a large hole pocket centered on the Brillouin zone and two neighboring electron pockets along the Γ –*X* direction[8–10,13]. The hole pocket is observed in angle-resolved photoemission spectroscopy (ARPES)[8–10], but is not apparent in SdH measurements[14]. Prominent quantum oscillations observed in the T_d phase arise from orbits associated with the electron pocket[14]. Figure 2a, b shows magnetoresistance and SdH oscillations at ambient pressure, in which these are clearly seen. As the fast Fourier transform (FFT) explicitly shows (Fig. 2c), the beating seen in Fig. 2b is due to two similar frequencies, $F_\alpha = 240.5$ T and $F_\beta = 258$ T, the result of symmetry-allowed spin–dorbit splitting. First-principles calculations identify these frequencies with the larger extremal $\mathbf{k}_z = 0$ cross sections of the electron pocket.

Modeling of the SdH oscillations yields a remarkably good fit (Fig. 2d) to the experimental SdH by the Bumps program[15] (Supplementary Figs. 15–23, Supplementary Table 5, Supplementary Notes 9 and 10). Notably, all of the oscillations feature a π Berry's phase[16], consistent with a Weyl topology (Supplementary Figs. 3–7, 14, and Supplementary Note 2). The effective band masses are light and slightly less than previously reported[14,17], as shown in Fig. 2e. As a function of pressure, the electron pockets increase modestly in size due to lattice compression, but the nontrivial phase shift is maintained throughout the T_d phase (Supplementary Tables 1–4). This trend is consistent with first-principles calculations as shown in Fig. 3a and b, which indicates the persistence of Weyl nodes up to 1.4 GPa (Supplementary Fig. 6 and Supplementary Note 2).

[1]NIST Center for Neutron Research, NIST, Gaithersburg, MD 20899, USA. [2]Center for Nanophysics and Advanced Materials, Department of Physics, University of Maryland, College Park, MD 20742, USA. [3]Department of Materials Science and Engineering, University of Maryland, College Park, MD 20742, USA. [4]Joint Quantum Institute, NIST and University of Maryland, College Park, MD 20742, USA. [5]Department of Physics, Washington University in St. Louis, St. Louis, MO 63130, USA. ✉email: ilin610@umd.edu; nbutch@umd.edu

Published in partnership with Nanjing University

npj nature partner journals

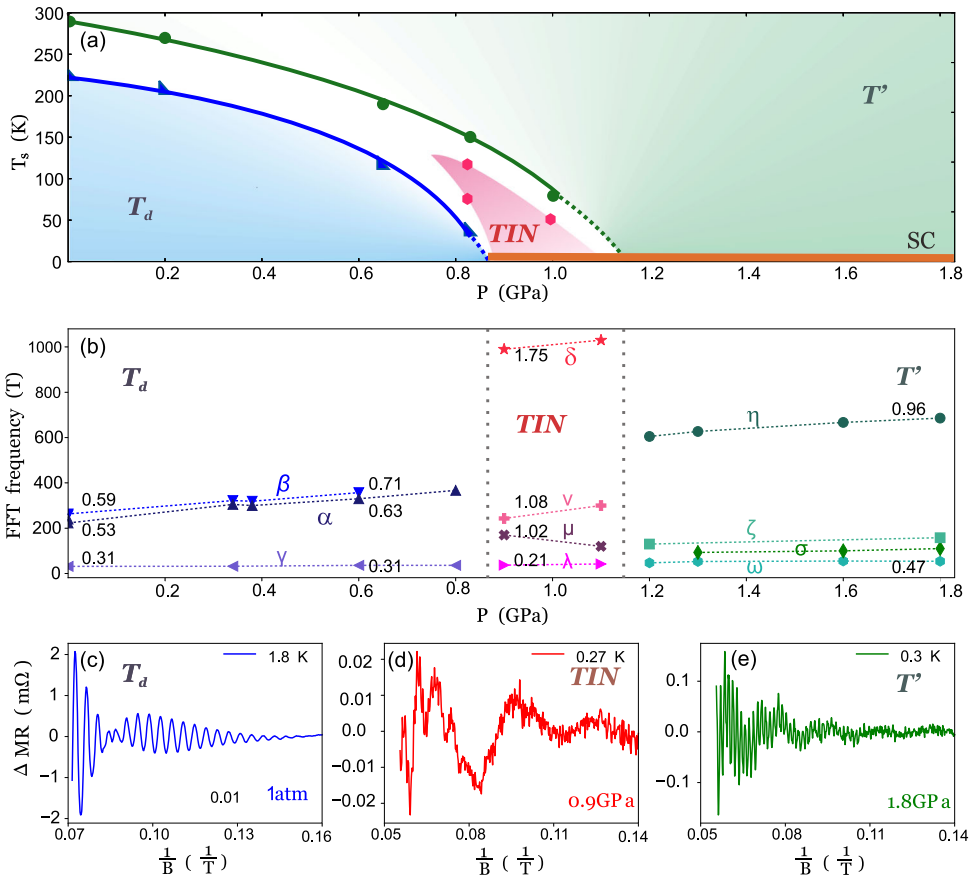

Fig. 1 Pressure–temperature phase diagram of $MoTe_2$. a Pressure–temperature phase diagram of $MoTe_2$. The green and blue symbols delineate the extent of 100% volume fraction of T' and T_d phases, respectively, determined through neutron scattering. The onset of full volume superconductivity coincides with the end of the T_d phase at 0.8 GPa [12], where a topological interface network (TIN) is observed. **b** Pressure dependence of the quantum oscillation frequency, with different branches labeled by Greek letters. The numbers correspond to the effective mass, which changes slightly with pressure. The quantum oscillations with the strongest pressure dependence, α and β in the T_d phase, and η in the T' phase, correspond to extremal orbits on the large electron pockets. In the TIN region, these disappear and are replaced by a completely distinct set of oscillations arising from topological interface states. Representative quantum oscillations (**c**) at ambient pressure (Weyl semimetal in T_d), **d** 0.9 GPa (TIN), and **e** 1.8 GPa (higher-order topology in T'). Clear changes in the quantum oscillations reflect significant changes in the electronic structure.

Monoclinic T′– $MoTe_2$

In the T′ phase at pressures of 1.2 GPa and greater, one main frequency F_η replaces the two frequencies F_α and F_β. The Fermi surface in the T′ phase closely resembles that of the T_d phase, with the exception that the centrosymmetry of the T′ phase nullifies the spin–orbit splitting of the bands that contribute to this electron pocket (Fig. 3d, e). This similarity leads to a common pressure dependence of the measured electron pocket frequency in both phases, consistent with the pressure evolution of the calculated Fermi surface (Fig. 3c, Supplementary Fig. 8, and Supplementary Tables 1–4). The main feature not captured by the calculations is a pronounced discontinuity in band structure between T_d and T′ phases due to the discontinuous **c** axis dilation at the structural transition, which is not modeled (Fig. 3c). Unexpectedly, our SdH oscillations analysis shows that a π Berry's phase also exists in the centrosymmetric T′ phase (Supplementary Table S6). After an ARPES study identified surface states in this phase[13], it was identified theoretically with an unusual type of nontrivial topological state[11]. Our results are consistent with this prediction, and further have the exciting implication that the high-pressure superconductivity in the T′ phase may be inherently topologically nontrivial, as suggested by μSR measurements at these pressures[18].

Natural topological interface network (TIN)

A structural mixed region exists over a range of pressures and temperatures in between the bulk T_d and T′ phases (Fig. 1a). It consists of an approximately balanced partial volume fraction of T_d and T′. We emphasize that no other structural phases or ordered superstructures are apparent from neutron diffraction measurements (Supplementary Figs. 1 and 2). It would, therefore, be expected that any measured SdH oscillations in the mixed region would consist of a superposition of T_d and T′ signals, but we do not observe oscillations from either phase. We conclude that the mixed region is sufficiently disordered that SdH oscillations from both the T_d and T′ phases are suppressed due to increased electron scattering.

In light of this, it is completely unexpected that a distinct set of SdH oscillations appears (Fig. 1b, d). This is a robust effect; the oscillations in the mixed phase always appear on both increasing and decreasing applied pressures through the critical range, over multiple cycles, confirming their intrinsic nature. A different band structure in the mixed region is inferred from the presence of frequencies corresponding to changed Fermi surfaces, and a change in effective mass and much weaker oscillation amplitude relative to bulk T_d and T′, as shown in Fig. 4a–f. These quantum oscillations reflect features typical of topologically protected states, namely, persistence in the presence of strong disorder, as

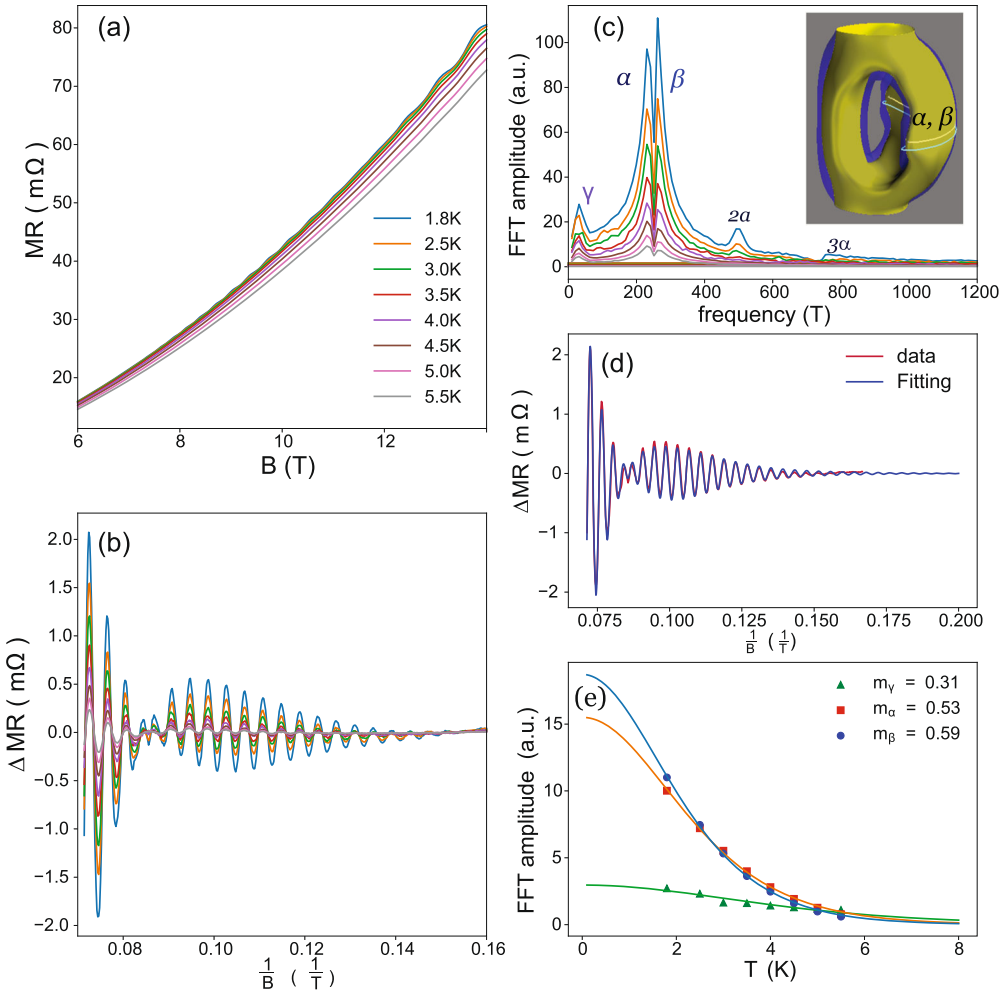

Fig. 2 Quantum oscillations in the magnetoresistance in $MoTe_2$ at ambient pressure. a The longitudinal MR of the bulk T_d-$MoTe_2$ measured at ambient pressure with a magnetic field parallel to the **c** axis. **b** The corresponding SdH oscillations after subtraction of a second-order polynomial background. **c** The fast Fourier transform (FFT) spectra show three Fermi surfaces with oscillation frequencies at $F_\gamma = 32.5$ T, $F_\alpha = 240.5$ T, and $F_\beta = 258$ T. The inset shows the α and β orbits on the calculated electron pocket. **d** Fit to the SdH oscillation at 1.8 K yield nontrivial Berry's phases $\phi_\gamma = \pi$, $\phi_\alpha = 0.88\pi$, and $\phi_\beta = 0.88\pi$. Details of the fit are discussed in the Supplementary Information. **e** The effective masses of the carriers are obtained through temperature-dependent Lifshitz–Kosevich fits.

well as π Berry's phases (Supplementary Tables 5 and 6). Because there are no additional structural phases in the mixed region, only T_d and T′, these topological states must be surface states of the bulk phases, which in this case, exist at their interfaces. Thus, the multiple natural interfaces stabilized in $MoTe_2$ by the first-order nature of the structural transition serve as the foundation for a completely different type of electronic system in $MoTe_2$: a natural topological interface network (TIN).

In the TIN, due to the layered structure of both T_d and T′ phases, the **ab** plane is preserved, and the largest grain boundaries fall along the **ab** plane, which is the orientation probed by the SdH measurements (Fig. 4g). In $MoTe_2$, a naturally generated heterostructure provides an interesting demonstration of topological transport protection. The lateral dimensions of the interfaces are the same as those of the bulk grains, based upon which one naively expects similar damping of the SdH oscillations from the interfaces. The absence of quantum oscillations from bulk T_d and T′ phases illustrates that the scattering from the TIN microstructure is significant for the bulk bands. Yet the clear SdH oscillations from the interfaces prove that the interfacial states have lower scattering than the bulk, and are a sign of their topologically nontrivial nature. In other words, the interfacial signal has been amplified by suppressing the bulk SdH oscillations through grain boundary scattering, and increasing the interface volume.

Density-functional theory (DFT) calculation of T_d–T′ slab model

First-principles calculations offer additional insight into the electronic structure of the TIN and its stability. We investigated a variety of possible mixed phases that might describe the mixed region, including T_d-like phases with different $MoTe_2$ stacking orders, periodic superstructures, and finite slabs of T_d and T′ phases and their interfaces as shown in Fig. 5a and b (detailed calculations are discussed in the Supplementary Figs. 9–13 and Supplementary Notes 4–6). Calculations demonstrate that the only model consistent with the experimentally determined high-frequency oscillations of ~1 kT (Fig. 4d) is a system consisting of only T_d–T′ interfaces, the TIN (Fig. 5d).

The Fermi-surface pockets associated with the interface are identified in two different but complementary calculations. Consider a periodic superstructure of T_d and T′ phases, as shown in Fig. 5a. Surprisingly, the T_d–T′ interface has lower energy if the $MoTe_2$ layers at the interface have the same type of Te distortion, labeled as L or R, compared to the L–R–L–R-type stacking order found in bulk T_d and T′ phases. Since L- or R-type planes cannot be

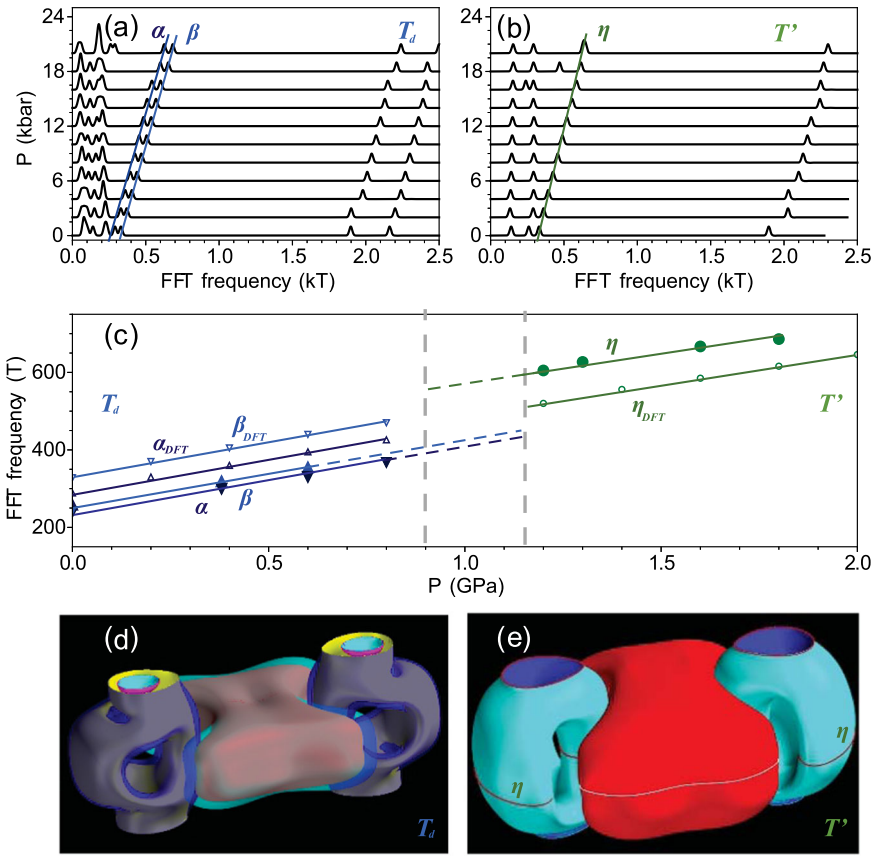

Fig. 3 Comparison between the calculated and experimental quantum oscillation frequencies for T_d and T′ phases. a, **b** Calculated in-plane quantum oscillation frequencies for the T_d and T' phases. The SdH oscillation frequencies arising from the electron pockets increase with the same pressure dependence in both phases. **c** A comparison between calculated and measured frequencies shows excellent quantitative agreement. The discontinuity in measured values is due to the jump in **c** axis dilation between phases. **d**, **e** Calculated bulk Fermi surfaces of the T_d and T' phases.

converted to each other by simply sliding the planes, this sort of interface presents a large energy barrier to the removal of stacking faults. The fact that this LL-type interface has lower energy than the interface with L–R stacking explains the stability of the mixed intermediate phase. Comparing the Fermi surfaces of the pure T_d and T′ phases with the T_d–T′ superstructure yields distinct Fermi-surface pockets with quantum oscillation orbits of 0.16 kT and 1.0 kT (bottom panel of Fig. 5d) in excellent agreement with our measurements.

Even though the periodic superstructure calculations of the T_d–T′ interface are consistent with the TIN model, the interface pockets have some dispersion due to interactions between the periodic images of the interface. To eliminate this effect, consider two slabs of T_d and T′ initially separated by about 9.5 Å (Fig.5b). These two slabs are brought together to form the T_d–T′ interface in a supercell where the combined T_d–T′ slab is separated by ~16.3 Å, large enough to avoid any image interactions (Fig. 5b, bottom). Comparing the Fermi surfaces of the isolated slabs (Fig. 5b) and combined slabs with the interface (shown in Fig. 5c), yields Fermi-surface pockets associated with the interface (Fig. 5d, top).

The agreement is excellent between the surface states from the periodic and finite slab calculations. These 2D quantum oscillation orbits are in impressive agreement with the experimental results (middle panel of Fig. 5d). Thus, the slab calculations directly link the observed high-frequency oscillation in the mixed region to interface states, as a TIN would produce.

DISCUSSION

Essential to any topological surface state is the meeting of two bulk phases with different topological invariants. A typical example is that of a Weyl semimetal interfaced with a topologically trivial vacuum, on whose boundary Fermi arcs are observed, as in T_d–$MoTe_2$[8]. In contrast, the second phase of the TIN is the topologically nontrivial T′ phase, which forms a large number of T_d/T′ interfaces due to the structural disorder. Then, for surface states to exist at these interfaces, there must be a change in topology between T_d and T′ phase, as expected for phases of Weyl and higher-order topological states. Although such interfaces have until now not received much theoretical attention, recent scanning tunneling microscopy measurements on $MoTe_2$ have suggested the existence of conducting hinge states in the T′/T_d domain wall at ambient pressure[19]. Our results did not directly observe 1D-hinge state, but cannot completely exclude the possibility of 1D paths. Our measurements and calculations show that 2D topological interfaces are also possible. Our discovery suggests that topological interfaces in 3D materials are a rich area for future exploration and exploitation.

Finally, we briefly discuss the relationship between the TIN and superconductivity in $MoTe_2$. Both the superconducting volume fraction and T_c increase dramatically at the same pressure at which the TIN is stabilized (Fig. 1a). Taking into further consideration the 2D nature of superconductivity, based on our previous calculations[12] and recent upper critical field measurements under pressure[20], a strong case is made that superconductivity is topologically nontrivial, consistent with previous claims from

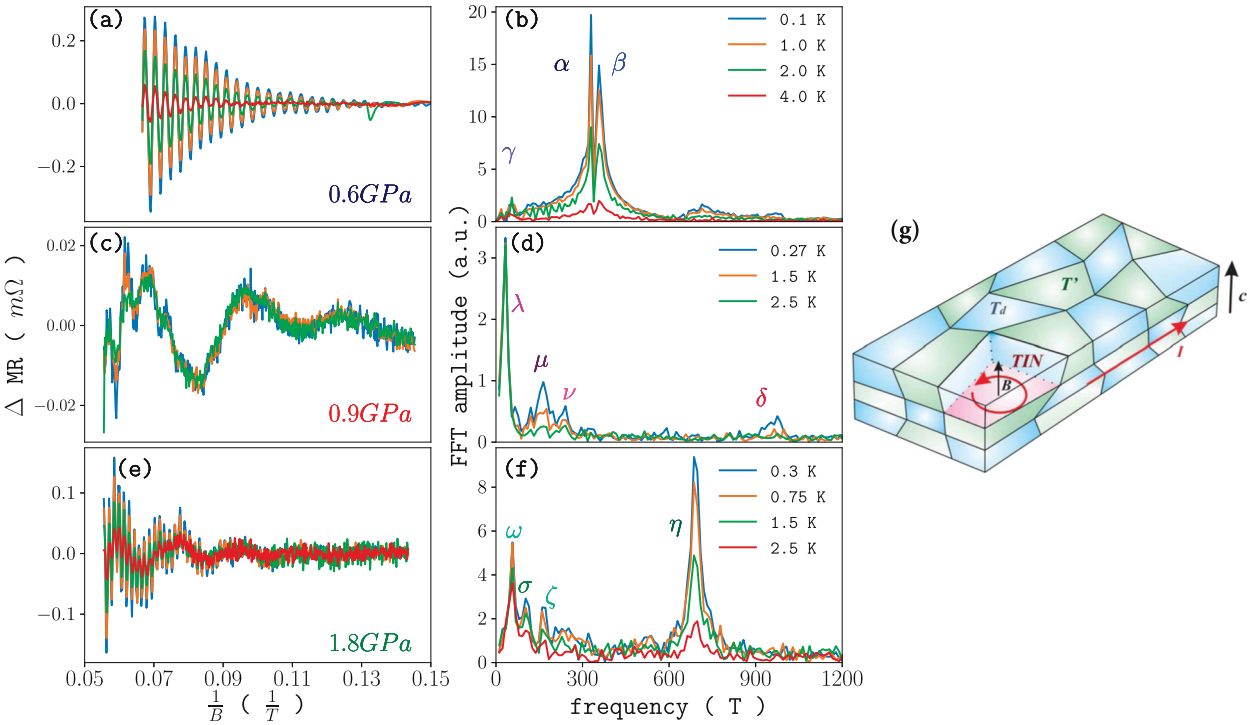

Fig. 4 Quantum oscillations in the magnetoresistance in $MoTe_2$ under pressure. Temperature dependence of the SdH oscillations of $MoTe_2$ measured at (**a**) 0.6 GPa in the T_d phase, (**c**) 0.9 GPa in the topological interface network (TIN), and (**e**) 1.8 GPa in the T' phase. Note the large changes in oscillation amplitude at different pressures. Corresponding fast Fourier transform (FFT) spectra of (**b**) T_d, (**d**) TIN, and (**f**) T' emphasize the dramatic changes in quantum oscillation frequency, due to changes in the dominant electronic orbits, as pressure tunes through the different phases. **g** Schematic of the topological interface network (TIN) showing the 3D mixed T_d–T' microstructure. The relatively weak but coherent signals are robust against pressure-induced disorder and only come from the connected interfaces between grains of T_d and T'. This TIN heterostructure can parametrically increase the number of surface channels and is a promising approach to increasing the surface-to-volume ratio of mixed-phase topological materials. The SdH signal is only related to cyclotron motion in the **ab** plane since electric current (**I**) and magnetic field (**B**) are along **a** and **c** crystallographic axis.

μSR measurements[18]. The combination of pressure-sensitive structure and topology in $MoTe_2$ makes this an exciting playground for the use of topological interfaces, with potential applications in a variety of quantum devices.

METHODS

First-principles calculations

The total energy, structure optimization under pressure, and band structure and Fermi-surface calculations were performed by Quantum Espresso[21], which is based on DFT, using a plane-wave basis set and fully relativistic all-electron projected augmented wave (PAW) potentials[22]. The 4s, 4p, 4d, and 5s electrons of Mo and the 4d, 5s, and 5p electrons of Te were treated as valence. We used 0.02 Ry Methfessel–Paxton smearing with wavefunction and charge density cut-off energies of 100 Ry and 800 Ry, respectively. The exchange-correlation interactions were described by the generalized gradient approximation (GGA) with the Perdew–Burke–Ernzerhof exchange-correlation functional[23]. The Brillouin-zone integration was performed using Monkhorst-Pack grids of special points with $16\times8\times4$ for total energy and structure optimizations and $32\times16\times8$ with tetrahedra method for electronic density of states and Fermi-surface calculations. The spin–orbit (SO) interactions and the weak inter-layer van der Waals (vdW) interactions were all included in our calculations. We used grimme-d2[24] vdW correction with parameter london —s6 = 0.6. The effect of electron correlations is included within DFT+U method with U = 3.0 eV for the Mo 4d-states. Including electron correlation brings the calculated band structure and Fermi surface into an excellent agreement with quantum oscillation and ARPES measurements, as discussed in Supplementary Information and also found in other very recent studies[25,26]. Fermi-surface sheets and SdH orbits are visualized by our custom python code using Mayavi[27]. The quantum oscillation frequencies/orbits and their angle dependence were calculated using the skeaf code[28].

Crystal synthesis

Large single crystals were grown using the Te self flux method described elsewhere[12] using high purity Mo powder (5N metals basis excluding W, Alpha Aesar), and Te shot (6N, Alpha Aesar). High sample quality has been confirmed by X-ray and neutron diffraction, stoichiometry has been confirmed by wavelength dispersive spectroscopy, and the samples measured have residual resistivity ratios >1000.

Structural measurements

Determinations of the temperature and pressure-dependent crystal structure were made using elastic neutron scattering measurements at 14.7 meV on the BT-4 triple-axis spectrometer at the NIST Center for Neutron Research using a collimation and filter setup of open-pg-40′-pg-s-pg-40′-120′, where pg refers to pyrolytic graphite. Single crystals were mounted in a steel measurement cell aligned in the $H0L_M$ zone, and He was supplied as a pressure medium to maintain hydrostatic pressure conditions as described elsewhere[12]. The T_d and T′ phases and their volume fractions were identified from the position and intensity of $(201)_M$ reflections, which both split in 2θ and shift in ω in the T′ phase. Rocking curves and ω–2θ scans were taken at each pressure and temperature. Scans along (00L) from (2 0 0.5) to (2 0 4.5) were also obtained at 0.8 GPa in all T_d or T′ condition, as well as in the mixed region at both 0.8 and 1 GPa to look for possible superstructure reflections. None were observed.

Transport measurements

A nonmagnetic piston-cylinder pressure cell was used for transport measurements under pressure up to 1.8 GPa, using a 1:1 ratio of n-Pentane to 1-methyl-3-butanol as the pressure medium and superconducting temperature of lead as pressure gauge at base temperature.

All transport measurements were performed on the same $MoTe_2$ crystal with 110-μm thickness using four-point contacts made with silver epoxy. The pressure dependence of the superconducting transition and structural

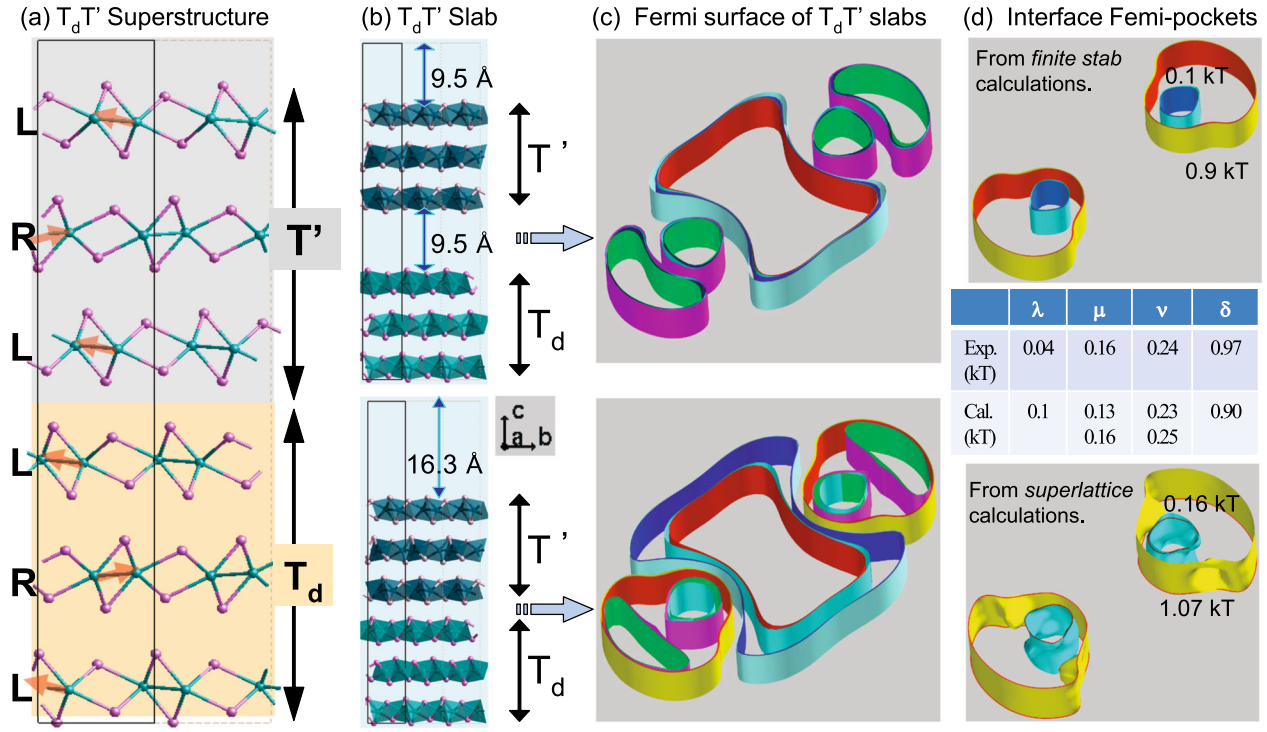

Fig. 5 The topological interface network T_d–T′ superstructure model. a Six layers of T_d–T' periodic superstructure, consisting of three layers of T_d and T' phases with L–L interface. **b** Three layers of T_d and T' slabs, separated (top) and joined (bottom). **c** Fermi surface obtained from separated (top) and joined slabs (bottom). **d**—top: The difference in the Fermi surfaces of the separated (**c**—top) and joined slabs (**c**—bottom), directly indicating the states due to the T_d–T' interface. Similarly, (**d**—bottom) shows the interface Fermi pockets from the periodic superstructure shown in (**a**). The middle panel in (**d**) shows the quantum oscillations from the T_d–T' joint slab calculations (**b**—bottom) compared with the experimental frequencies, which are represented as Gaussian curves with equal but arbitrary intensities.

transition[12] were determined in a Quantum Design PPMS and dilution refrigerator in the first pressure run (1 atm to 1.8 Gpa and back to 1 atm). The SdH oscillations were measured in a PPMS and dilution refrigerator (only 0.6 Gpa) in the second pressure run (1 atm to 1.8 Gpa and back to 1 atm) and in an Oxford Instruments Heliox at 0.3 K and 6–18 T in a third pressure run (pressure range below 1.8 Gpa). The identification of commercial equipment does not imply endorsement by NIST.

DATA AVAILABILITY

Data are available from the authors upon reasonable request.

Received: 5 March 2020; Accepted: 14 August 2020;
Published online: 07 September 2020

REFERENCES

1. Kitaev, A. Y. Fault-tolerant quantum computation by anyons. *Ann. Phys.* **303**, 2–30 (2003).
2. Nayak, C. et al. Non-Abelian anyons and topological quantum computation. *Rev. Mod. Phys.* **80**, 1083–1159 (2008).
3. Qi, Y. et al. Superconductivity in Weyl semimetal candidate $MoTe_2$. *Nat. Commun.* **7**, 11038 (2016).
4. Qian, X., Liu, J., Fu, L. & Li, J. Quantum spin Hall effect in two-dimensional transition metal dichalcogenides. *Science* **346**, 1344–1347 (2014).
5. Hsu, Y.-T., Vaezi, A., Fischer, M. H. & Kim, E.-A. Topological superconductivity in monolayer transition metal dichalcogenides. *Nat. Commun.* **8**, 14985 (2017).
6. Li, Y. et al. Nontrivial superconductivity in topological $MoTe_{2-x}$ S_x crystals. *Proc. Natl Acad. Sci. USA* **115**, 9503–9508 (2018).
7. Soluyanov, A. A. et al. Type-II Weyl semimetals. *Nature* **527**, 495–498 (2015).
8. Deng, K. et al. Experimental observation of topological Fermi arcs in type-II Weyl semimetal $MoTe_2$. *Nat. Phys.* **7**, 1105–1110 (2016).
9. Huang, L. et al. Spectroscopic evidence for type II Weyl semimetallic state in $MoTe_2$. *Nat. Mater.* **15**, 1155–1160 (2016).
10. Jiang, J. et al. Signature of type-II Weyl semimetal phase in $MoTe_2$. *Nat. Commun.* **8**, 13973 (2017).
11. Wang, Z. et al. Higher-order topology, monopole nodal lines, and the origin of large Fermi arcs in transition metal dichalcogenides XTe_2 (X = Mo, W). *Phys. Rev. Lett.* **123**, 186401 (2019).
12. Heikes, C. et al. Mechanical control of crystal symmetry and superconductivity in Weyl semimetal $MoTe_2$. *Phys. Rev. M.* **2**, 074202 (2018).
13. Crepaldi, A. et al. Persistence of a surface state arc in the topologically trivial phase of $MoTe_2$. *Phys. Rev. B* **95**, 041408 (2017).
14. Rhodes, D. et al. Bulk Fermi surface of the Weyl type-II semimetallic candidate γ -$MoTe_2$. *Phys. Rev. B* **96**, 165134 (2017).
15. Kienzle, P. Bumps: curve fitting and uncertainty analysis (Version 0.7.10). Preprint at http://readthedocs.org/projects/bumps/downloads/pdf/latest/ (2018).
16. Murakawa, H. et al. Detection of Berryas phase in a bulk Rashba semiconductor. *Science* **342**, 1490–1493 (2013).
17. Luo, X. et al. T_d -$MoTe_2$: a possible topological superconductor. *Appl. Phys. Lett.* **109**, 102601 (2016).
18. Guguchia, Z. et al. Signatures of the topological s^{+-} superconducting order parameter in the type-II Weyl semimetal T_d -$MoTe_2$. *Nat. Commun.* **8**, 1082 (2017).
19. Huang, F.-T. et al. Polar and phase domain walls with conducting interfacial states in a Weyl semimetal $MoTe_2$. *Nat. Commun.* **10**, 4211 (2019).
20. Hu, Y. J. et al. Angular dependence of the upper critical field in the high-pressure 1T′ phase of $MoTe_2$. *Phys. Rev. M* **3**, 034210 (2019).
21. Giannozzi, P. et al. Quantum espresso: a modular and open-source software project for quantum simulations of materials. *Matter* **21**, 395502 (2009).
22. Kresse, G. & Joubert, D. From ultrasoft pseudopotentials to the projector augmented-wave method. *Phys. Rev. B* **59**, 1758–1775 (1999).
23. Perdew, J. P., Burke, K. & Ernzerhof, M. Generalized gradient approximation made simple. *Phys. Rev. Lett.* **77**, 3865–3868 (1996).
24. Grimme, S. Semiempirical GGA-type density functional constructed with a long-range dispersion correction. *J. Comp. Chem.* **27**, 1787–1799 (2006).
25. Xu, N. et al. Evidence of Coulomb-interaction-induced Lifshitz transition and robust hybrid Weyl semimetal in T_d -$MoTe_2$. *Phys. Rev. Lett.* **121**, 136401 (2018).

26. Aryal, N. & Manousakis, E. Importance of electron correlations in understanding the photo-electron spectroscopy and the Weyl character of $MoTe_2$. *Phys. Rev. B* **99**, 035123 (2019).
27. Ramachandran, P. & Varoquaux, M. 3d visualization of scientific data. *IEEE Comput. Sci. Eng.* **13**, 40–51 (2011).
28. Rourke, P. M. C. & Julian, S. R. Numerical extraction of de Haas-van Alphen frequencies from calculated band energies. *Comp. Phys. Commun.* **183**, 324–332 (2012).

ACKNOWLEDGEMENTS

We thank Jay D. Sau, Paul Kienzle, and Daniel J. Campbell for helpful discussions. We specially appreciate John Singleton for the thorough discussion on the analysis of the g factor and Berry phase in Lifshitz–Kosevich (LK) formula. The computational work was performed using the NIST Enki high-performance computer cluster. This work utilized facilities supported in part by the National Science Foundation under Agreement No. DMR-0454672 and NCNR/UMD Cooperative Agreement 70NANB15H261. Experimental measurements at the University of Maryland were supported by DOE through Grant No. DE-SC-0019154, and materials synthesis by the Gordon and Betty Moore Foundation's EPiQS Initiative through Grant No. GBMF4419. Portions of the experimental research were supported by NIST.

AUTHOR CONTRIBUTIONS

I.L., C.E., and T.M. performed transport measurements. C.H. and W.R. measured neutron scattering. N.P.B., C.H., and S.R. synthesized materials. T.Y. performed electron band structure calculations and theoretical analysis. I.L., T.Y., C.H., and N.P.B. wrote the paper with contributions from all authors.

COMPETING INTERESTS

The authors declare no competing interests.

ADDITIONAL INFORMATION

Supplementary information is available for this paper at https://doi.org/10.1038/s41535-020-00264-8.

Correspondence and requests for materials should be addressed to IL.L. or N.P.B.

Reprints and permission information is available at http://www.nature.com/reprints

Publisher's note Springer Nature remains neutral with regard to jurisdictional claims in published maps and institutional affiliations.

Quantum oscillations from networked topological interfaces in a Weyl semimetal Supplemental Material

I-Lin Liu[1,2,3], Colin Heikes[1,4], Taner Yildirim[1], Chris Eckberg[2], Tristin Metz[2], Hyunsoo Kim[2], Sheng Ran[1,2,3,5], William Ratcliff II[1], Johnpierre Paglione[2], and Nicholas P. Butch[1,2]

[1]*NIST Center for Neutron Research, NIST, Gaithersburg, MD 20899, USA.*
[2]*Center for Nanophysics and Advanced Materials, Department of Physics, University of Maryland, College Park, MD 20742 USA.*
[3]*Department of Materials Science and Engineering, University of Maryland, College Park, MD 20742 USA.*
[4]*Joint Quantum Institute, NIST and University of Maryland, College Park, MD 20742, USA*
[5]*Department of Physics, Washington University in St. Louis, St. Louis, MO 63130, USA*

(Dated: August 13, 2020)

CONTENTS

A. Supplementary Note 1: Elastic neutron scattering

The stated relationship between quantum oscillations and crystal structure is based on our pressure and temperature dependent elastic neutron scattering measurements. As described in our previous work[1], we determine the T_d and T' phase fractions from the scattering intensity at the (201) reflections of the monoclinic unit cell for the T' phase. For the T_d phase, this is for a unit cell with a β-angle of 90^0. The scattered intensity is determined from the integrated intensity of transverse scans centered at the nominal peak positions for each phase. We used the BT-4 triple-axis spectrometer at the NIST Center for Neutron Research with a monochromatic 14.7 meV neutron beam and a collimation and filter geometry of Open-pg-40'-pg-s-pg-40'-120 where pg refers to an oriented pyrolytic graphite filter used to remove higher order neutrons. The temperature dependent integrated intensity of each phase, taken upon warming, is given in Fig. 1(a)-(c) at 0.3 GPa, 0.8 GPa, and 1 GPa respectively. Figs. 1(d)-(f) show the raw scattering data fit to a Gaussian peak shape used to extract the integrated intensity for the three different temperature regimes seen at 0.8 GPa. In the mixed region, the temperature dependent isobars show a clear deviation from normal mean field-like behavior expected for a first order phase transition. We attribute this to kinetic trapping of the structural phase transition.

Critical to our discussion of phase coexistence and our interpretation of the cause of the arrested transition is that despite an apparent suppression of a phase transition temperature to zero temperature at a specific pressure, we do not believe this should be described as a quantum structural phase transition. We attribute the effective "freezing" of the transition to the reduction of the structural transition temperature into a temperature regime where thermal fluctuations cannot overcome the energy barrier between the phases. We can draw an analogy between this behavior and the kinetic freezing observed in the low temperature first order magnetic transitions in (La,Pr,Ca)MnO_3 between a ferromagnetic and charge-ordered antiferromagnetic state[2]. In the magnetic case the complex energy landscape is attributed to competition between magnetic order, structural and chemical disorder, and inter-grain strain, which is consistent with other observations of similar transistions in magnetocaloric materials with magnetostrictive coupling[3]. Given the previously established sensitivity of the $MoTe_2$ structural phase transition to pressure and strain as well as the known structural disorder in van der Waals materials, it is reasonable to assume that inter-grain strain and disorder may dominate the phase transition kinetics in this system as well[1,4]. At 0.8 GPa where we first observe a broad mixed region, the transition temperature is still high enough that it is possible to undercool the sample such that it eventually completes the phase transition, but at 1 GPa the transition temperature is further suppressed and no sufficient undercooling is possible leading to the mixed region as the ground state structure.

Given the coherent oscillations in the mixed region, we considered whether this could be evidence of a new bulk structural phase driven by stacking disorder during the phase transition. If this were the case, we would expect to observe new reflections along the stacking direction. We performed [00L] scans along [20L] at 0.8 GPa at temperatures corresponding to the T_d phase and the mixed region. These are shown in figure 1. Clearly we see no evidence of new reflections that would indicate a new phase, instead observing only integer L peaks for the T_d phase, split integer peaks from both monoclinic twins in the T' phase, and scattering attributable to the mixed phase in the mixed region. While we cannot completely rule out a new intermediate meta-stable phase, we see no indication of this either from superlattice reflections along [00L] or from missing intensity in the mixed region. The same is seen at 1.5 K and 1 GPa, with a slightly different ratio of T_d to T' phase, consistent with the volume fractions extracted from the (201) scans used for the phase diagram in figure 2.

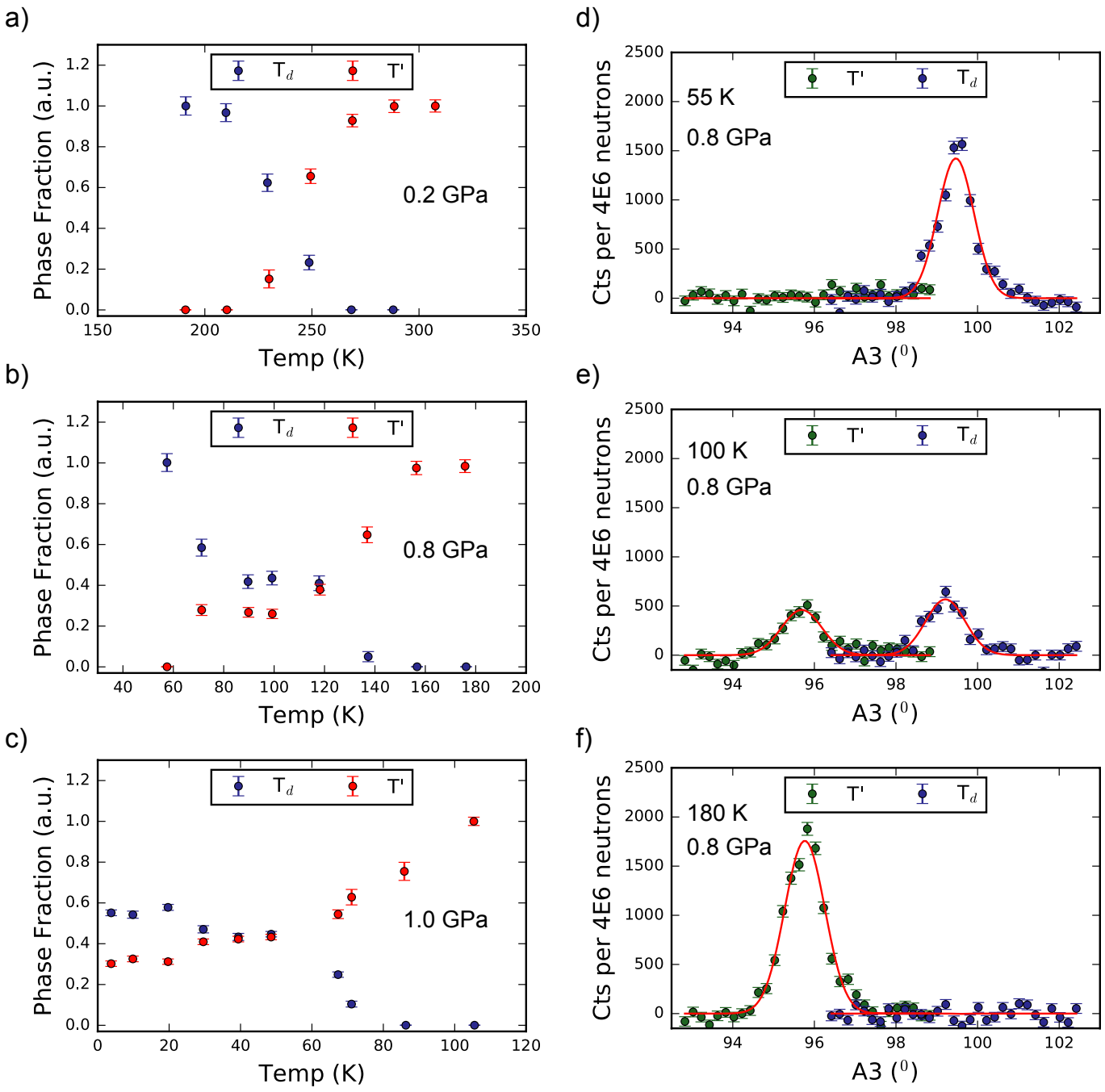

Supplementary Figure 1: **Temperature evolution of T' and T_d phase fractions.** a-c shows the temperature dependent phase fractions of both the T' and T_d phases at three different pressures illustrating the mixed region above 0.6 GPa. d-f show the background subtracted scattering intensities at the (201) peak positions in the pure T_d phase, the mixed region, and in the pure T' phase used to extract the phase fractions for the 0.8 GPa data in panel (b). The red lines show the Gaussian fits to the data used to extract the integrated peak intensities for phase fraction determination. Error bars correspond to an uncertainty of one standard deviation.

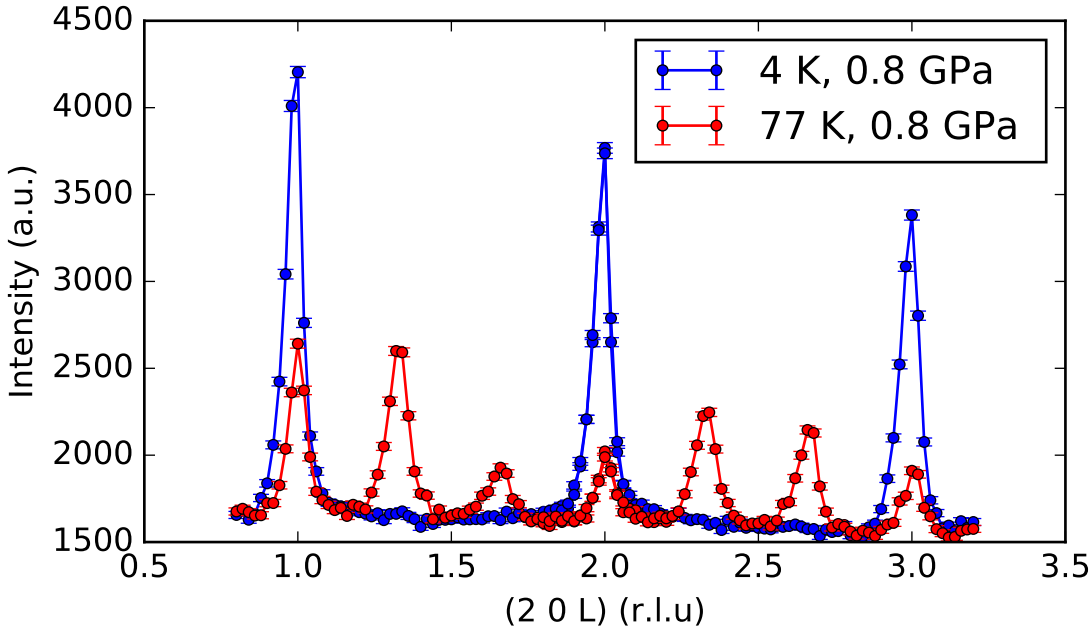

Supplementary Figure 2: **Scans along (20L) taken at 0.8 GPa showing scattering along L in the T_d phase and in the mixed region.** In the mixed region, we see no new scattering that would be indicative of stacking order along the **c**-axis, observing only clear reflections from both the T_d and T' phases.

B. Supplementary Method: First-Principles Calculations

In this section, we discuss the details of our first-principles electronic structure calculations of $MoTe_2$ as a function of pressure for both 1T'- and T_d-phases, respectively. The total energy, structure optimization under pressure, and band structure and Fermi surface calculations were performed using Quantum Espresso,[5], which is based on density-functional theory (DFT), using a plane wave basis set and fully relativistic all-electron projected augmented wave (PAW) potentials[6,7]. The 4s, 4p, 4d, and 5s electrons of Mo and the 4d, 5s, and 5p electrons of Te were treated as valence electrons. We used 0.02 Ry Methfessel-Paxton smearing, with wavefunction and charge density cut-off energies of 100 Ry and 800 Ry, respectively. The exchange-correlation interactions were described by the generalized gradient approximation (GGA) with the Perdew-Burke-Ernzerhof exchange-correlation functional[8]. The Brillouin-zone integration were performed using Monkhorst-Pack grids of special points with dimensions of $16 \times 8 \times 4$ for total energy and structure optimizations and $32 \times 16 \times 8$ for electronic density of states and Fermi surface calculations using the tetrahedron method. The spin-orbit (SO) interactions and the weak inter-layer van der Waals (vdW) interactions were all included in our calculations. We used the grimme-d2[9] vdW correction with parameter london - s6 = 0.6. The effects of electron correlations are included within the DFT+U method with U =3.0 eV for the Mo 4d-states. Including electron-correlation brings the calculated band structure and Fermi-surface into excellent agreement with Quantum Oscillation and ARPES measurements as found in very recent studies[10,11]. Fermi-surface sheets and SdH orbits are visualized by our custom python code using Mayavi[13]. The quantum oscillation frequencies/orbits and their angle dependence were calculated using the skeaf code[14].

C. Supplementary Note 2: Effect of Electron Correlations on the Band Structure and Fermi Surface of $MoTe_2$

Recent studies[10,11] found that electron correlations are essential for a precise description of the bulk electronic structure of T_d-$MoTe_2$ as reFealed by angular resolved photoemission spectroscopy (ARPES)[10] and the angular dependence of the Fermi surface by quantum oscillation (QO) experiments[11]. Hence, in our study we adopted DFT+U scheme to describe the electron correlations within the Mo 4d-states. The overall best agreement with ARPES and QO data is obtained for U =3 eV[10,11], which was also used in our calculations in this study.

Figures 3 and 4 show the effect of the Hubbard U (taken as 3.0 eV) on the band structure and the Weyl-points in the T_d- and 1T'-phases of $MoTe_2$, respectively. A detailed study of the effect of Hubbard U on the Weyl point (WP) in $MoTe_2$ can be found in Ref[11]. Briefly, in total there are four pairs of WPs, each in one quadrant, all of which are located on the $\mathbf{k}_z = 0$ plane and are related by the crystal symmetry. In our fully self-consistent calculations where both the lattice parameters and atomic positions were obtained self consistently from structure optimization, we usually get two Weyl points at ($\pm\mathbf{k}_x$, $\pm\mathbf{k}_y$,0) with very small $\mathbf{k}_y$.

We note that the biggest effect of including U is to shift the bands near the Y-point so that there is no longer a small electron pocket at the Fermi surface as shown in Fig. 5. The other main effect is to lower some of the bands further below the Fermi level

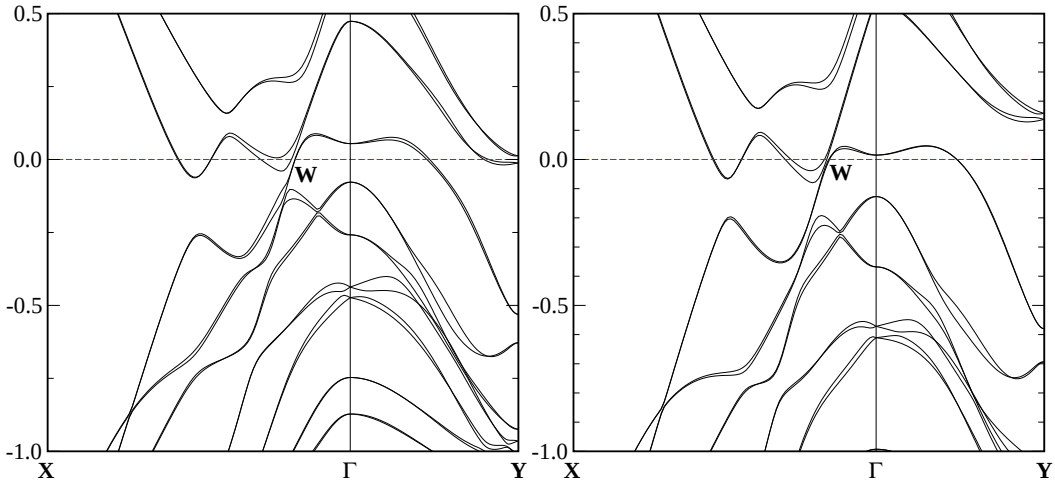

Supplementary Figure 3: **Band structure of T_d-phase of bulk $MoTe_2$.** Electronic band structure without (left) and with Hubbard U (right), showing the effect of the electron correlations on the band structure. The main effect is to shift up the bands near Fermi level around the Y-point while the Weyl point (shown as "w") is not effected by U. The small splitting of the bands is due to Spin-Orbit (SO) coupling and the lack of inversion symmetry in the T_d phase.

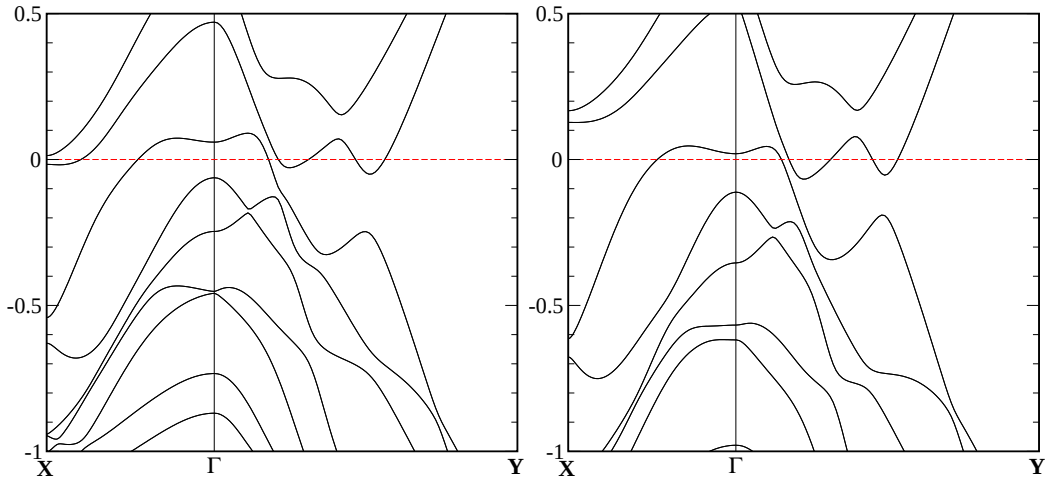

Supplementary Figure 4: **Band structure of 1T'-phase of bulk $MoTe_2$.** Band structure with (right) and without U term (left) in 1T'-phase of bulk $MoTe_2$. The effect of SO coupling is still important even though it does not split the bands (but shifts them around to affect the Fermi Surface).

which does not have any effect on the Fermi surface. It is important to note that the Weyl point near the Fermi level remains unaffected by the inclusion of the Hubbard correlation term U in our calculations. However, as we shall see below, including U is critical to explain the pressure dependence of the QO frequencies that we have measured in this study.

Finally, Figure 6 shows the effect of pressure on the Weyl point. The main effect of pressure is to shift up the hole pocket while shifting down the electron pocket near the Fermi level such that the Weyl point roughly does not change with initial applied pressure, at least up to 14 kbar. At higher pressure, it seems that the Weyl point moves slightly above the Fermi level (Fig. 6). A HOTI in the T_d phase requires the annihilation of the Weyl nodes[12], therefore, we would not expect HOTI in T_d in our system here.

In our calculations, besides the Hubbard term U, there are other parameters such as lattice constants and atomic positions that we need to determine. Calculations can be based on the experimental parameters or the parameters can be determined self consistently within the DFT+U structural optimization at any given pressure. Figure 5 shows the Fermi surface of T_d- and 1T' phases of $MoTe_2$ for both experimental and DFT optimized structures with and without electron correlation effects (i.e. U). We note that the Fermi surface is very sensitive to the lattice parameters and the atomic positions. Our optimized lattice parameters and atomic positions are within 1% of the experimental values as shown in Tables 1 and 2. The biggest variation is in the **a**-axis for the T_d phase and it is 1.4%. Despite this excellent agreement between experiment and calculations, the difference in the Fermi surface between experimental and the optimized structures is quite large. In order to be self-consistent, we decided to use optimized lattice parameters and atomic positions for a given pressure as obtained from our DFT+U calculations. In this way, we are able to determine the pressure dependence of the Fermi Surface and determine the quantum oscillation orbits and frequencies. The only free-parameter in our DFT+U calculations is the Hubbard U, which was shown to be around U =3 eV for $MoTe_2$ to match the ARPES measurements as well as the angle dependence of the QO frequencies[10,11].

D. Supplementary Note 3: Pressure Dependence of the Fermi Surface and Quantum Oscillations

In this section, we present our results related to the pressure dependence of the Fermi surface and quantum oscillation orbits as a function of applied pressure for both phases of $MoTe_2$. In both phases, we calculate similar Fermi surfaces and orbits which are summarized in Figure 7. Near zone center Γ, we have a square-box hole-like Fermi surface (red). The orbit around this Fermi surface is shown in Fig.7 as "s". Then, we have an electron-like Fermi surface with a shape of a coffee mug (light blue). This shape has basically three types of extremal orbits as shown in the Figure 7. We label the orbits at the opening as "op". Then, the orbit near the handle like surface as "h". And, finally we have the orbits near the cup like surface denoted as "c". As we shall see below, this orbit is sensitive to pressure and we identified this orbit as in our quantum oscillation measurements. Finally, we have a small pocket of squashed elliptical surface (dark blue), which we call the "e" orbit. In the case of T_d-phase, these orbits have two counterparts due to SO-splitting.

We have carried out full structure optimization at a given pressure and then calculated the Fermi surface over a dense k-grid to determine the orbit frequencies using skeaf code[14]. Our results are summarized in Tables 3 and 4. We note that most of the orbit-frequencies do not change much with applied pressure but the cup-orbit frequency increases with increasing pressure. As discussed in the main text, the slope of the frequency increase with pressure is in excellent agreement with the observed shifts

Supplementary Table 1: **Lattice parameters and fractional positions of T_d-$MoTe_2$.** Lattice parameters and fractional atomic positions as determined by our neutron diffraction measurements and our DFT+U calculations for T_d-$MoTe_2$ ($Pmn2_1$).

Experimental Structure			
a=3.46464 Å, b=6.30716 Å		c=13.84310 Å	90^o 90^o 90^o
Mo	0.000000000	0.606100004	0.497243989
Mo	0.500000000	0.393899996	0.997243989
Mo	0.000000000	0.029300001	0.014242000
Mo	0.500000000	0.970700018	0.514242010
Te	0.000000000	0.865899961	0.653545972
Te	0.500000000	0.134100020	0.153545972
Te	0.000000000	0.641099962	0.112019999
Te	0.500000000	0.358900000	0.612019999
Te	0.000000000	0.287699989	0.857258999
Te	0.500000000	0.712299993	0.357259033
Te	0.000000000	0.214699994	0.401510016
Te	0.500000000	0.785300043	0.901509982
DFT+U Optimized Structure			
a=3.51242 Å, b=6.33797 Å		c=13.80214 Å	90^o 90^o 90^o
Mo	0.000000000	0.596570039	0.499028659
Mo	0.500000000	0.403429961	0.999028659
Mo	0.000000000	0.043489108	0.012956972
Mo	0.500000000	0.956510911	0.512956982
Te	0.000000000	0.854056153	0.653752430
Te	0.500000000	0.145943828	0.153752430
Te	0.000000000	0.649980885	0.109058347
Te	0.500000000	0.350019077	0.609058347
Te	0.000000000	0.302836245	0.858321051
Te	0.500000000	0.697163737	0.358321085
Te	0.000000000	0.203297619	0.402703515
Te	0.500000000	0.796702418	0.902703481

in the experimental measurements. Hence, we identified this orbit as the one probed in our quantum oscillation measurements.

The topology of the Fermi surface pretty much stays the same with applied pressure up to 16 kbar (i.e. 1.6 GPa). Due to the reduction of the lattice constants the band overlap gets larger with increasing pressure, which in turn increases the orbit frequencies. However, at pressures larger than 1.6 GPa, due to strong inter-layer interaction, the hole-band with the square box shape starts to have an opening at the top/bottom of the box-surface as shown in Figure 8. For comparison, we show the Fermi surface at 20 kbar for both phases in Fig. 8 but we note that at these pressures, the main phase is the 1T' phase which is inversion symmetric. Interestingly the new orbit at the top of the hole-square band has about the same oscillation frequency as the cup-orbit near 0.65 kT.

Supplementary Table 2: **Lattice parameters and fractional positions of T'-$MoTe_2$.** Lattice parameters and fractional atomic positions as determined by our neutron diffraction measurements at 300 K and our DFT+U calculations for T'-$MoTe_2$ ($P2_1/m$).

Experimental Structure			
a=6.3281 Å, b= 3.4770 Å		c=13.021 Å	90^o 93.882^o 90^o
Mo	0.182799990	0.250000000	0.008300000
Mo	0.817199966	0.750000017	0.991700002
Mo	0.319399986	0.750000017	0.506199997
Mo	0.680599966	0.250000000	0.493799979
Te	0.587999989	0.250000000	0.106399996
Te	0.411999994	0.750000017	0.893599938
Te	0.096600004	0.750000017	0.149299988
Te	0.903399993	0.250000000	0.850699971
Te	0.557100023	0.750000017	0.351300002
Te	0.442900004	0.250000000	0.648699974
Te	0.056299998	0.250000000	0.395299983
Te	0.943700035	0.750000017	0.604699925
DFT+U Optimized Structure			
a=6.3422 Å, b=3.5106 Å		c=13.8292 Å	90^o 93.8907^o 90^o
Mo	0.181248302	0.250000000	0.007402050
Mo	0.818751654	0.750000017	0.992597952
Mo	0.320793055	0.750000017	0.506405748
Mo	0.679206897	0.250000000	0.493594228
Te	0.589309059	0.250000000	0.103197530
Te	0.410690924	0.750000017	0.896802404
Te	0.097660263	0.750000017	0.147835158
Te	0.902339734	0.250000000	0.852164801
Te	0.559332448	0.750000017	0.352629203
Te	0.440667579	0.250000000	0.647370773
Te	0.057121356	0.250000000	0.396415521
Te	0.942878677	0.750000017	0.603584387

Supplementary Table 3: **QO Frequencies (kT) in T_d-$MoTe_2$ phase as a function of pressure (kbar).** The orbit labels are defined in Figure 7.

Orbits	0 kbar	2 kbar	4 kbar	6 kbar	8 kbar	10 kbar	12 kbar	14 kbar	16 kbar	18 kbar	20 kbar
h1	0.14	0.15	0.15	0.155	0.16	0.163	0.167	0.17	0.174	0.17	0.17
h2	0.1	0.10	0.10	0.11	0.11	0.104	0.11	0.12	0.116	0.12	0.18
op1	0.235	0.23	0.21	0.22	0.21	0.22	0.21	0.21	0.210	0.204	0.19
op2	0.22	0.22	0.21	0.207	0.20	0.20	0.19	0.19	0.196	0.186	0.18
c1	0.33	0.37	0.405	0.44	0.470	0.506	0.57	0.57	0.601	0.653	0.684
c2	0.294	0.33	0.36	0.395	0.426	0.455	0.51	0.51	0.542	0.600	0.626
e1	0.08	0.06	0.06	0.055	0.06	0.05	0.046	0.045	0.05	0.056	0.04
e1	0.08	0.08	0.08	0.07	0.07	0.07	0.06	0.06	0.06	0.056	0.06
s1	1.90	1.9	1.98	2.01	2.04	2.07	2.10	2.13	2.15	2.21	0.26-2.24
s2	2.16	2.2	2.24	2.27	2.30	2.33	2.36	2.39	2.41	2.42	0.29-2.5

Supplementary Table 4: **QO Frequencies (kT) in T'-$MoTe_2$ phase as a function of pressure (kbar).** The orbit labels are defined in Figure 7.

Orbits	0 kbar	2 kbar	4 kbar	6 kbar	8 kbar	10 kbar	12 kbar	14 kbar	16 kbar	18 kbar	20 kbar
h	0.14	0.132	0.136	0.14	0.144	0.147	0.150	0.151	0.152	0.154	0.153
op	0.33	0.29	0.293	0.291	0.294	0.294	0.295	0.291	0.291	0.292	0.292
c	0.26	0.36	0.392	0.425	0.457	0.489	0.520	0.556	0.5854	0.616	0.646
s	1.896	2.027	2.030	2.10	2.130	2.160	2.185	2.245	0.24-2.25	0.47-2.27	0.63-2.3

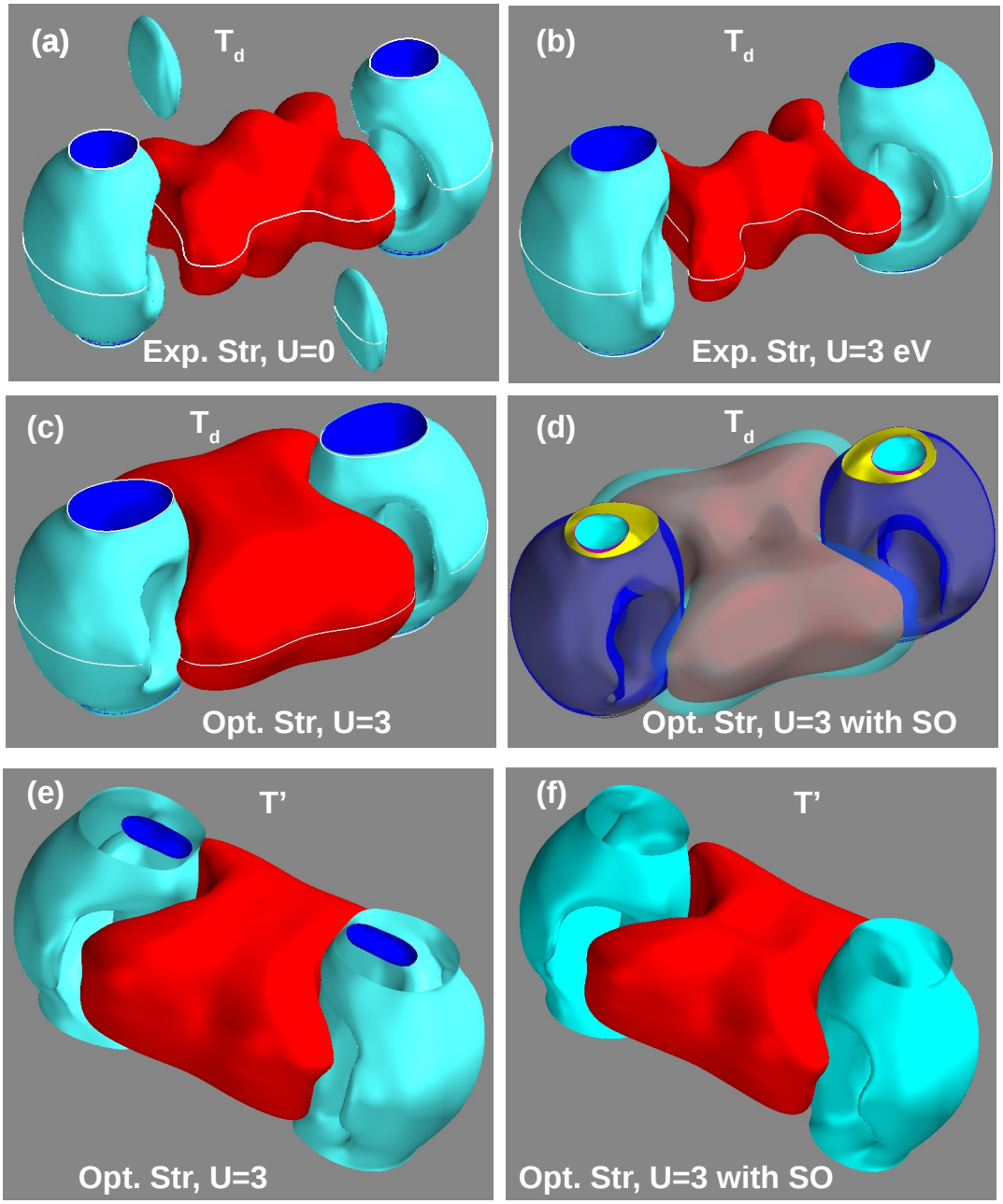

Supplementary Figure 5: **Fermi surface plots of $MoTe_2$.** Fermi surface plots of $MoTe_2$ for various cases; (a) Experimental structure with and without a U term; (b) Experimental structure with U = 3 eV; the main effect of which is to remove the (cyan) electron pockets near the Y-point; (c) Fully optimized structure with U =3 eV; Note that it is quite different than the one from the experimental structure shown in b; (d) Fully optimized structure with U = 3 eV and also with spin-orbit (SO) coupling; The main effect of spin-orbit coupling is to shrink and expand the surfaces so that they split; Note the significant shrinkage of the surface shown as dark blue color; (e-f) shows the Fermi surface in the 1T' phase with optimized structure and U =3 eV. Due to inversion symmetry, there is no splitting of the Fermi surface in the 1T'-phase but the bands are shifted around and the resulting Fermi surface is different. Also note that the small electron packet (dark blue in (e)) is removed with the inclusion of SO coupling (f).

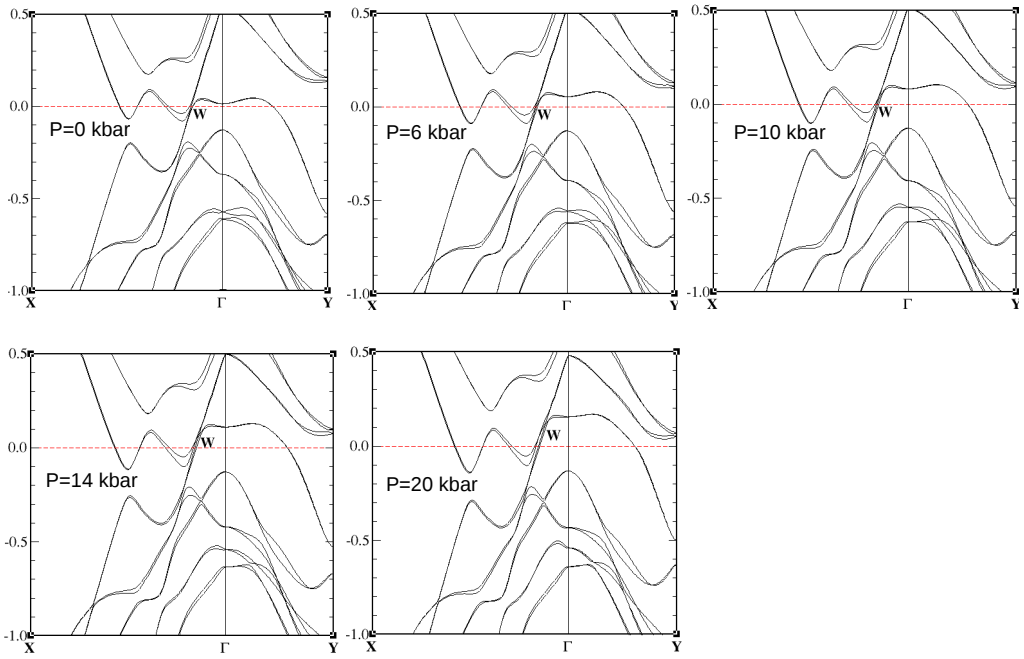

Supplementary Figure 6: **pressure dependence of electronic band structure of T_d-$MoTe_2$.** Electronic band structure with Hubbard U =3.0 eV as a function of applied pressure, showing the effect of pressure on the Weyl point shown as "w". The main effect is to shift up the energy of the hole-pocket while shifting down the electron-pocket near the Fermi level such that the Weyl point is roughly invariant under applied pressure, at least up to 14 kbar.

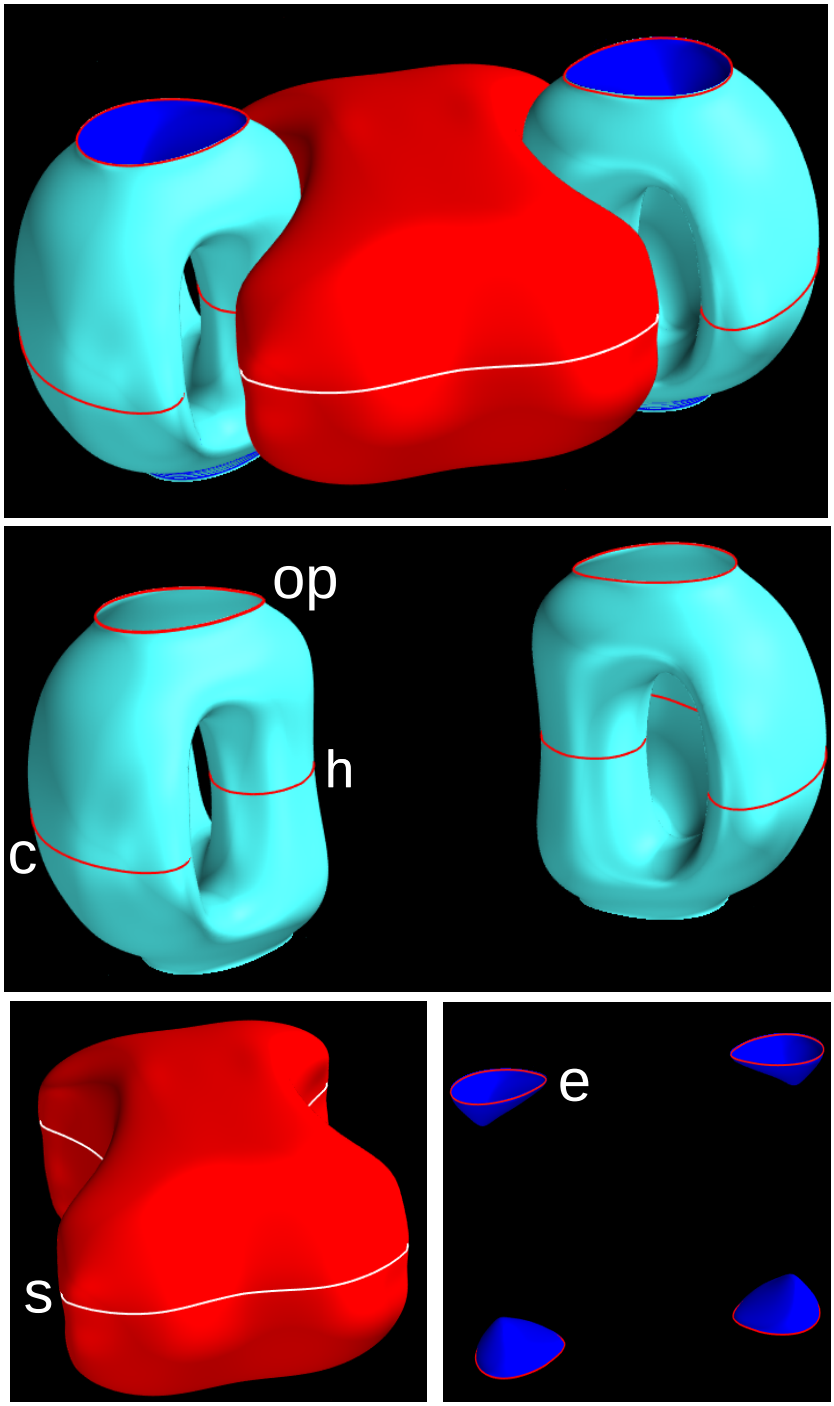

Supplementary Figure 7: **Fermi surface plots of carrier pockets in $MoTe_2$.** Top panel shows the main shape of the Fermi surface in both phases of $MoTe_2$, which consists of three types of bands; The red one is a square like box shape with mainly hole-character. We denote the orbits around this surface as "s". The main portion of the Fermi surface is electron-like and has a coffee mug shape (light blue). This shape supports three possible extreme orbits as shown as "op" (which is at the opening of the surface), as "h" which is the orbit around the handle like shape, and "c" which is the orbit around the cup portion of the Coffee Mug-shaped Fermi surface. Interestingly, this cup-like shape is the most sensitive to the pressure and the frequency of this orbit increases with increasing pressure, in excellent agreement with our measurements. Finally, we have a small pocket of electron Fermi surface (dark blue), which has an ellipsoidal shape and is therefore denoted as "e".

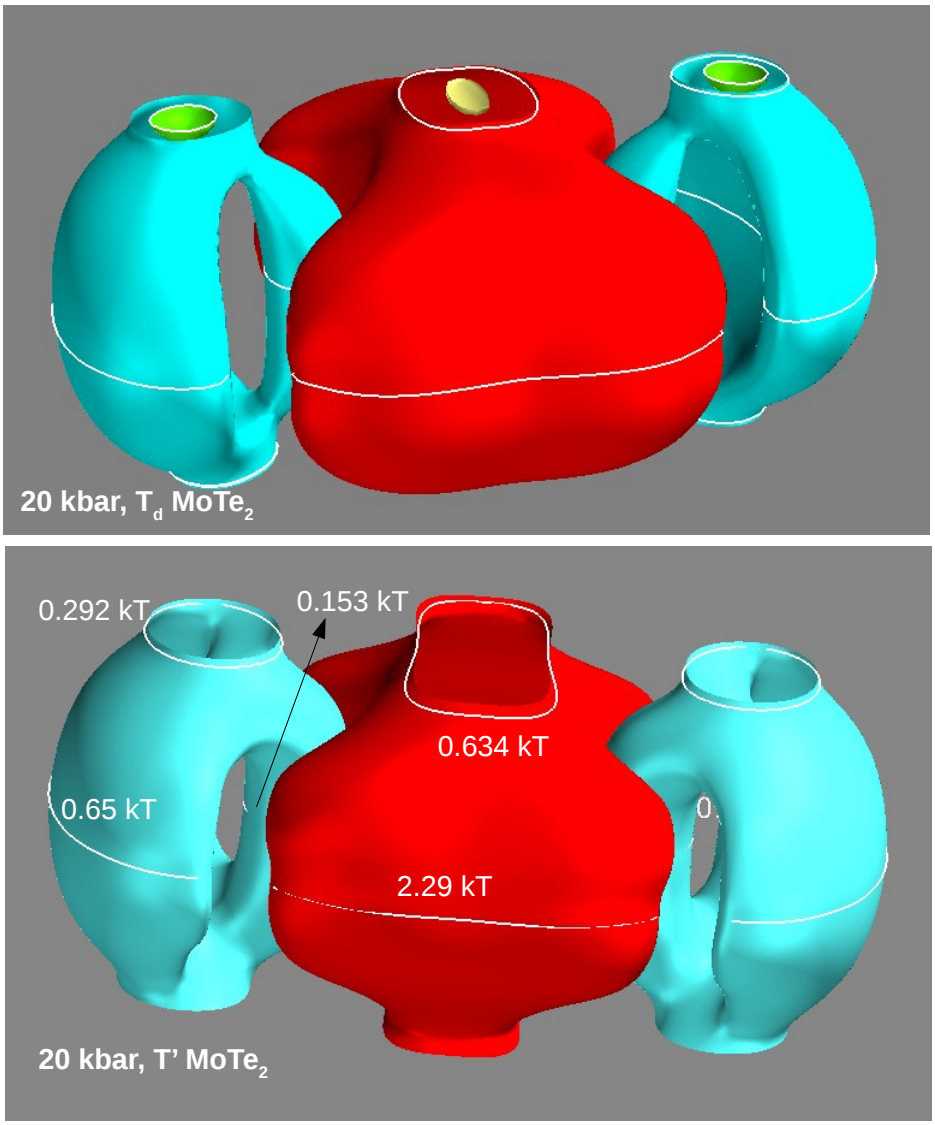

Supplementary Figure 8: **Fermi surface of $MoTe_2$ at 20 kbar pressure for T_d phase (top) and for 1T'-phase (bottom).** Note that the center square-box like Fermi surface starts to open at the top with orbit frequencies near 0.65 kT, which is similar to the cup-site orbit.

E. Supplementary Note 4: Fermi Surface Pockets and Quantum Oscillations from T_d-T' interface

In this section, we will consider different systems to see if we can reproduce quantum oscillations with frequency near 1 kT as experimentally observed at the intermediate pressure mixed region.

It is of interest to see what kind Fermi surface and quantum oscillation we have from a finite layers of $MoTe_2$ as these could be indication of some surface states or maybe the decoupled few layers of $MoTe_2$ during the experiments. Hence, we have performed DFT calculations for single, double and triple layers of T_d-$MoTe_2$ and look at the quantum oscillations from them. The calculations were done fully self consistently where both atomic positions and lattice parameters were optimized. We used the same cutoff and k-grid as discussed above. The spin-orbit interactions were also included. We used a super-cell with **c**-axis of 20 Ang, which is large enough to minimize the image interactions due to periodic structure.

Figure 9 shows the supercell structures with one, two, and three layers of T_d-$MoTe_2$ and the corresponding Fermi surfaces. In the case of single layer, we have two types of Fermi surfaces; two electron pockets with 0.14 kT orbits and the central hole pocket

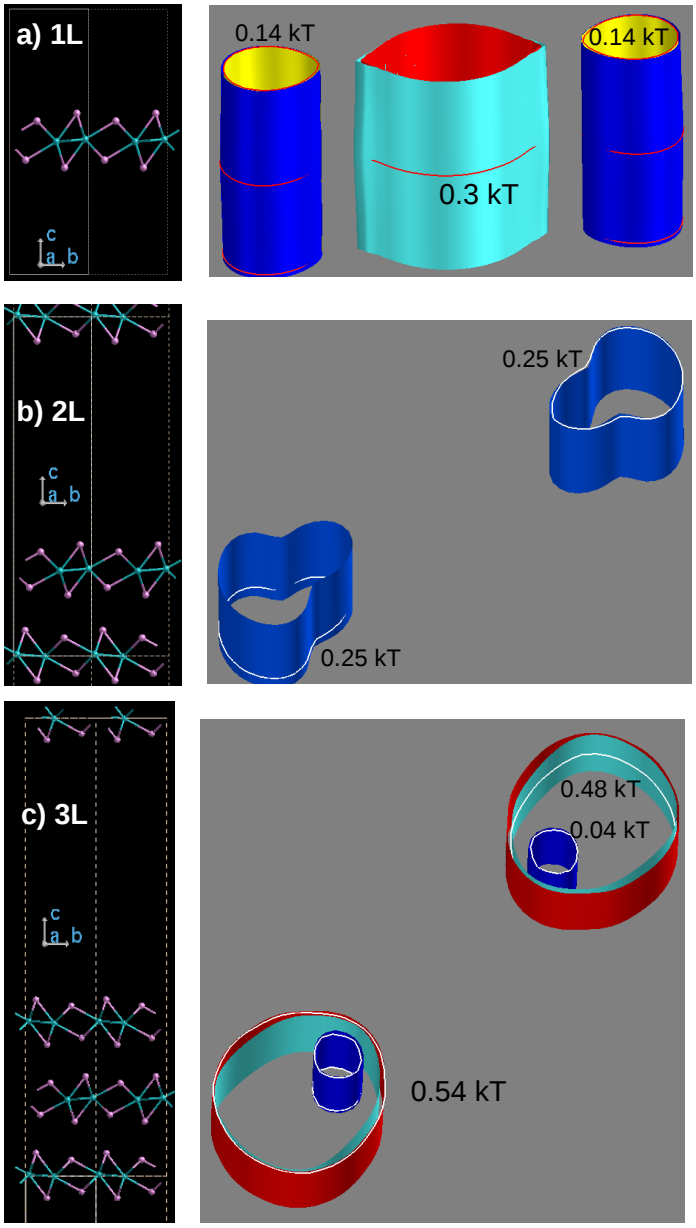

Supplementary Figure 9: **Supercell structure in $MoTe_2$ with variant layers of T_d-$MoTe_2$.** Supercell structure of $MoTe_2$ with one layer (a), two layers (b) and three layers (c) of T_d-$MoTe_2$ and the corresponding Fermi surfaces. The quantum oscillation frequencies and the orbits are also shown for each case.

with 0.3 kT orbit. These electron and hole pockets are the foundation of the Weyl points present in these systems. However, as shown in Figure 9, the Fermi surface is very sensitive to the number of $MoTe_2$ layers present. In the case of double layer, the hole pocket is pushed down below the Fermi level and only two electron pockets remains. As we shall see below the shape of the Fermi surface from double layer is quite similar to the interface state but the orbits are about twice smaller than 1kT as experimentally observed.

The Fermi surface of three layers of $MoTe_2$ is very different; it has cylindrical electron surfaces with oscillation orbits of 0.48-0.54 kT and small pocket with orbit of 0.04 kT. Based on these few layers of $MoTe_2$, it is very unlikely that the observed quantum oscillations at the intermediate phase could be due to surface state or from somehow decoupled few layers of $MoTe_2$.

F. Supplementary Note 5: Unsuccessful interface models

We first discuss hypothetical T_d-like structures with different stacking orders of the $MoTe_2$ planes as a possible source of the observed quantum oscillations near 1 kT. As discussed in detail in our previous work[1], the origin of T' and T_d phases is based on how the $MoTe_2$ planes are stacked on each other. The phase transition is basically driven by the lowest energy phonon mode which is related to **b**-axis displacement of the $MoTe_2$ planes with respect to each other. As shown in Figure 10, sliding one plane along the **b**-axis in the T_d phase indicates that there is another local minimum in the potential energy and this is related to the T' phase. Both the energy barrier and energy difference between these two stacking configurations is very small and because of that it is quite likely that we have many stacking faults during the T'-T_d phase transition. Hence, one may wonder how the stacking faults would affect the Fermi surface and is it possible that the observed oscillation near 1 kT could be due to dislocated $MoTe_2$ planes?

In order to test this idea, we calculated the band structure and the Fermi surface of a $MoTe_2$ phase where the middle plane is shifted by about 0.32 Å along the **b**-axis which corresponds to the 2nd local minimum in the potential. This new structure is almost degenerate with the T_d phase. However, the Fermi surface obtained in this phase is very similar to the perfect T_d phase as shown in Fig. 5d with some additional holes on the fermi surface. The quantum oscillation frequencies from this hypothetical $MoTe_2$ phase are at 0.2 kT, 0.6 kT and near 1.8 kT (hole pocket). Hence, the dislocation of $MoTe_2$ plane can not explain the experimentally observed high frequency quantum oscillation near 1 kT.

We next consider another type of stacking fault as shown in Figure 11. We note that in the perfect T_d phase, the $MoTe_2$ planes are stacked in a fashion that the Te-distortion is characterized by left (L) and right (R) displacements alternatively as shown in

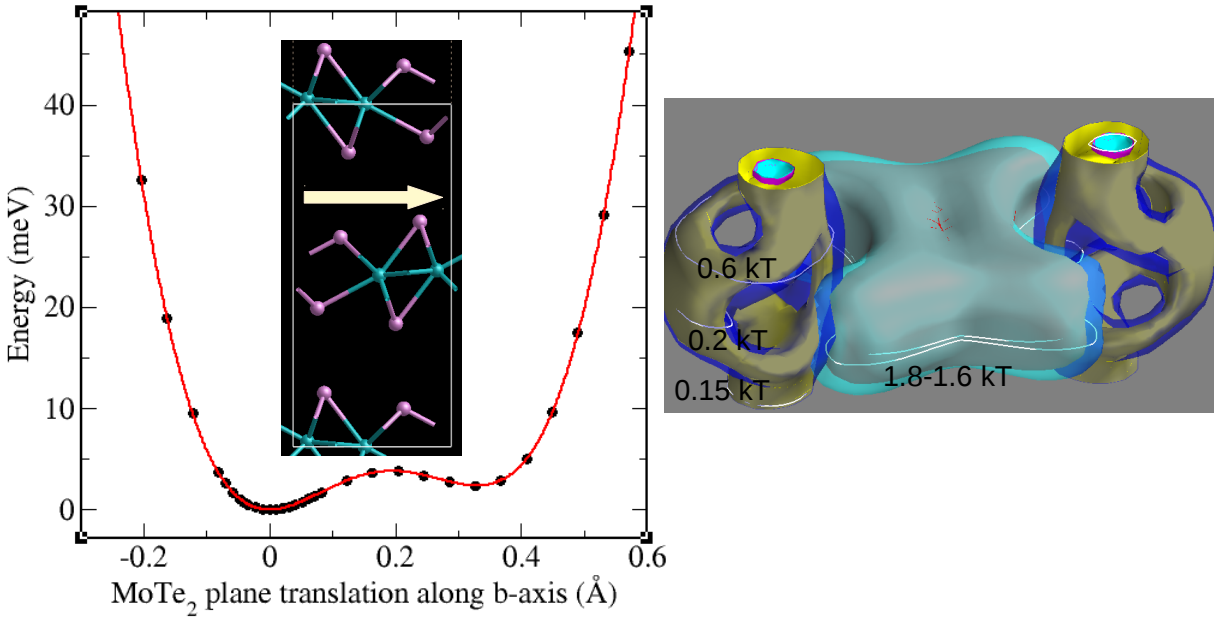

Supplementary Figure 10: Left: Total energy as the middle plane of MoTe2 slides along the **b**-axis, indicating the presence of the 2nd local minimum. Since the potential barrier is very low and the energies are very close we expect to see many stacking faults in $MoTe_2$. Right: Fermi surface from the structure where the middle plane is at the 2nd local minimum. The Fermi surface is very similar to the $MoTe_2$ phase with T_d structure. Hence, this sort of stacking fault cannot explain the observed quantum oscillation near 1 kT.

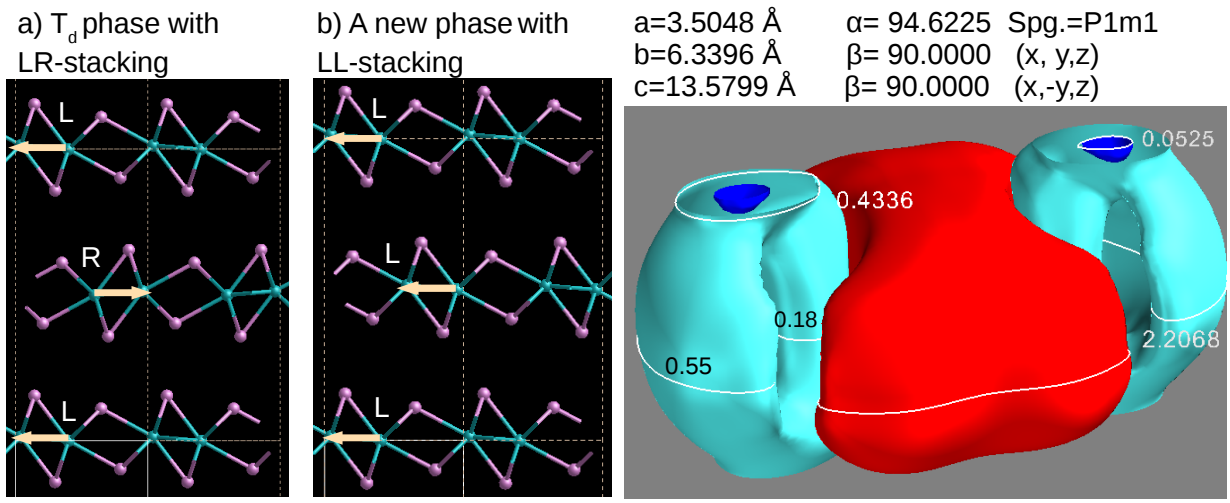

Supplementary Figure 11: **Hypothetical structure of left-distorted stacking T_d-$MoTe_2$.** A hypothetical structure of $MoTe_2$ obtained by stacking left-distorted $MoTe_2$ planes taken from T_d phase. The inset shows the optimized lattice parameters as well as the Fermi surface with orbits for quantum oscillations.

Fig 11. Converting an "R" type $MoTe_2$ plane to "L" type cannot be accomplished by simply sliding the plane, because to go from "L" type to "R" type, the Te atoms have to move. Based on our initial reaction path calculations, there is no easy path to go from "L" to "R" plane. Hence, this sort of stacking fault is much more difficult to remove compared to a sliding dislocation. We construct a hypothetical $MoTe_2$ phase by rotating the middle plane to convert it from "R" to "L" orientation, labeling the new phase as T_d-LL which is shown in Fig. 11. When we did full structure optimization in this stacking order of $MoTe_2$ planes, we obtained a distorted structure with cell angle of about 94.6 °. The Fermi-surface of this hypothetical structure is shown in the right panel of Fig. 11. The Fermi surface is very similar to that of ideal T_d or T' phases where the available orbits are around 0.18 kT, 0.55 kT, and 2.2 kT. This structure does not yield any Fermi surface pocket with quantum oscillation near 1 kT. Hence, this stacking of $MoTe_2$ layers can not explain the observed quantum oscillations near 1 kT either.

To summarize, several models based on $MoTe_2$ stacking faults failed to explain the observed 1 kT quantum oscillation. We also checked the Fermi surface of single, double or triple layers of $MoTe_2$, none of which has a Fermi surface pocket that gives a 1 kT quantum oscillations.

G. Supplementary Note 6: Successful interface model

In order to show that we only get quantum oscillations near 1 kT when there is an interface between T_d and T' phases, we now consider supercell structures that contain both T_d and T' phases. Since the T' phase has a lattice angle of $\approx 93.4^o$, we first confirmed that changing this angle to 90^o does not affect the Fermi surface significantly. Once the cell angles are all 90^o, creating a supercell that contains both T_d and T' phase is straightforward. We used the lattice parameters of the T_d phase at 10 kbar and created a supercell of six layers. We then took the top three layers out and put in three layers of T' phase. We then performed full structure optimization until the forces on all atoms were smaller than 0.01 eV/Ang, including those atoms at the interface. We used 64x32x3 k-point grids to calculate the Fermi surface.

While building a superlattice of T_d and T' phases, there can exist two types of interfaces depending on how the $MoTe_2$ planes stack together. We note that in both T_d and T' phases, the Mo atoms move towards the right ("R") or left "L" to lower the local symmetry and the planes are stacked to keep "R"-"L"-"R"-"L" sequence. Hence, when there is an interface between T_d and T'-phases, we could keep this stacking order as shown on the left panel of Fig. 12. We call this the LR-type interface. This kind of interface should be easily converted to either T_d or T' phase during the structural phase transition because sliding $MoTe_2$ planes from one minimum to the other does not cost too much energy and the energy barrier for sliding is very small. Hence we did not consider this type of interface further.

The other possibility for the interface is to match the T_d and T' phase such that the R-L-R-L stacking ordering is not maintained. This creates a case where there is either L-L or R-R stacking at the interface as shown on the right panel of Figure 12. We note that eliminating this interface is not trivial. Converting a "L"-oriented $MoTe_2$ plane to a "R" oriented plane can not be

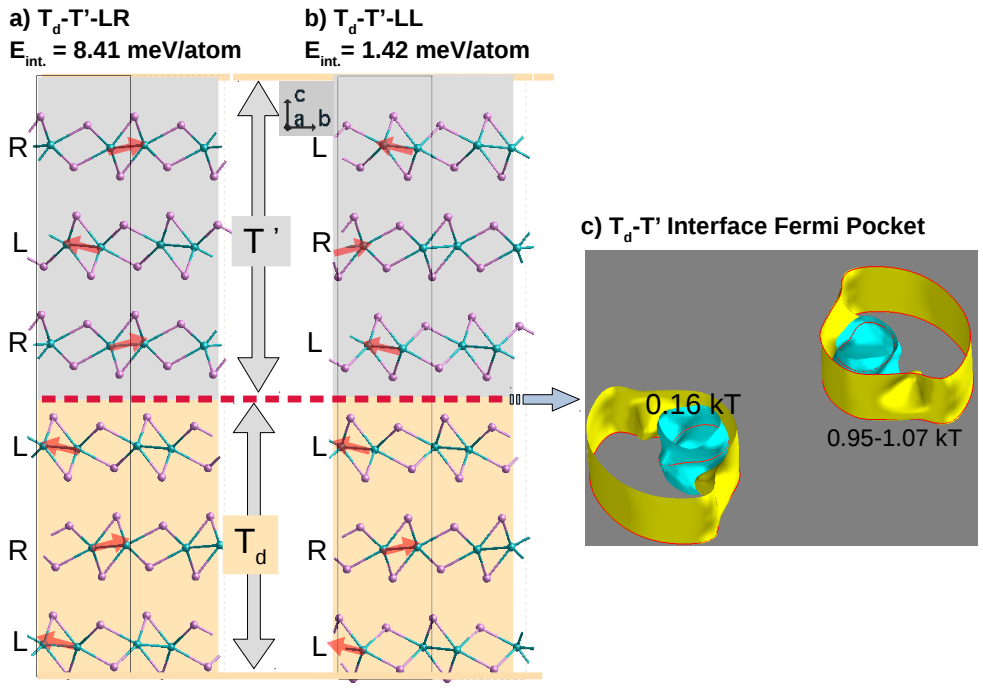

Supplementary Figure 12: **Interface superlattice structures of T_d/T' $MoTe_2$.** Interface superlattice structures consisting of 3 layers of T_d $MoTe_2$ and 3 layers of T' $MoTe_2$ with two possible interfaces; (a) LR-interface where the stacking pattern of "R" and "L" is preserved as in the case of pure T' and T_d phases; (b) RR-interface where there is no easy path with a low energy barrier to convert the interface to LR or RL stacking order. Interestingly this interface is 7 meV/atom lower in energy than the LR-type interface. The new Fermi surface pockets from the LL-interface yield quantum oscillations orbits with frequencies of approximately 1 kT and 0.2 kT, respectively. These are in close agreement with the experimentally observed oscillations at the intermediate phase, supporting our picture of TIN phase.

achieved by a simple sliding of the plane as in the case of the LR-type interface. Mo atoms have to move to change the R to L orientation. DFT reaction-path calculations estimate that the potential barrier for the R–T transition is of the order of 0.5 eV, which is quite large. Hence, this sort of interface or domain wall will be more difficult to anneal out during the phase transition. Probably both Mo and Te atoms move in a cooperative way to lower the potential barrier.

In order to understand the energy of the two types of interface further, we calculated the interface interaction energy which is defined as

$$En(\text{interface}) = En(\text{T}_\text{d} - \text{T}'\text{supercell}) - (En(\text{T}_\text{d}) + En(\text{T}'))/2 \quad (1)$$

The calculated interface energy for both the LR-type interface and the LL-type interface are given in Figure 12. Both interface formation energies are positive, meaning that converting the T_d-T' mixed phase into a single phase of either T_d or T' is energetically more favorable. To our surprise, the LL-type interface actually has a 7 meV/atom lower energy than the LR-type interface. Hence, between the two possible interfaces, the LL-type interface is energetically favored. This explains why we experimentally observe a mixed phase between the T_d and T' phase transition, as eliminating this interface requires passing through a large energy barrier and is therefore not trivial.

We next calculated the Fermi surface of the T_d-T' supercell as shown in Figure12. Comparing the Fermi surfaces with a perfect 6L superlattice, we determine new states that are shown in the right panel of Figure 12. The larger one has a quantum oscillation orbit at 0.95-1.07 kT, which is in excellent agreement with the measurements peformed in the intermediate phase. We also have a small Fermi pocket with quantum oscillation near 0.15 kT, which is close to several low frequency oscillations below 0.2 kT observed experimentally. These Fermi surfaces are mainly two dimensional but there is some dispersion along the **c**-axis as evidenced by the features on the Fermi surface. This small dispersion is due to the finite size of the unit cell, which is about 41.4 Å, almost too large for DFT calculations but not large enough to avoid small interactions between the images of the periodic cell.

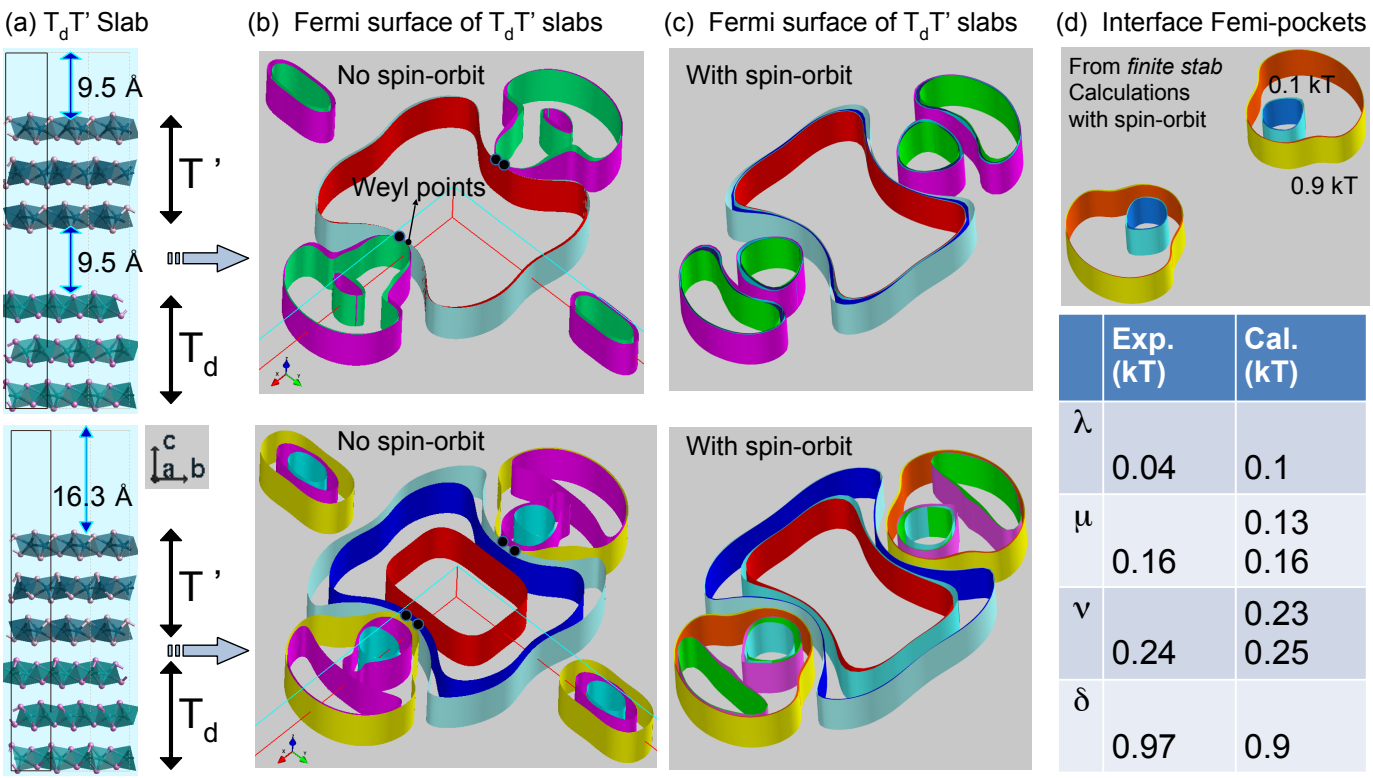

	Exp. (kT)	Cal. (kT)
λ	0.04	0.1
μ	0.16	0.13 0.16
ν	0.24	0.23 0.25
δ	0.97	0.9

Supplementary Figure 13: **The topological interface network T_d-T' superstructure model.** (a) Three layers of T_d and T slabs when they are separated (top) and joined (bottom). In each case, atomic positions were fully optimized. Fermi surface obtained from separated and joined slabs without spin-orbit interactions (b) and with spin orbit interactions included (c). The difference in the Fermi surfaces of the separated (top) and joined slabs (bottom) directly gives the states associated with the T_d-T'interface which is shown in (d). The bottom panel in (d) shows the quantum oscillations from the T_d-T' joined slab calculations compared with the experimental frequencies.

Even though the periodic superstructure calculation discussed above establishes that the observed quantum oscillation at 1 kT is due to the T_d-T' interface, it does not demonstrate the interface states clearly, due to significant interactions along the **c**-axis and complications due to folding of the bands in the Brillion zone because of the supercell periodicity. To more clearly compare the interface Fermi surface to that of the bulk, we performed a similar calculation but this time we put together the three layers of T_d and three layers of T'-phases as slabs rather than as a periodic superstructure as shown in Figure 13. In this way, we bring the T_d and T'-slabs towards each other to form the T_d and T' interface. By comparing the Fermi surface of the separated T_d and T' slabs with that of joined T_d-T' slab, we are able to directly identify the interface states.

Figure13a shows the separated (top) and joined (bottom) T_d-T' slabs, respectively. We used the lattice parameters of the $MoTe_2$ T_d phase at 10 kbar (i.e. 1GPa) pressure. The **c**-axis of the cell is taken about 4 times the size of **c**-axis of T_d phase at 10 kbar. This gives about 9.5 Å vacuum when the three layer slabs are separated and 16.3 Å vacuum when they are joined. All the atomic positions were optimized until total forces on atoms are less than 0.01 eV/Å. Once we had the optimized positions, we carried out Fermi surface calculations using 64x34x1 k-point grids with and without spin orbit interactions. The resulting Fermi surfaces are plotted in Fig.13. The main effect of the spin-orbit interaction is similar to the case of the bulk; The small Fermi pockets near (0,$\mathbf{k}_y$,0) are pushed below the Fermi level and other bands are split; As in the case of the bulk pure T_d phase, we have two pairs of Weyl points near ($\pm\mathbf{k}_x$,0,0). Comparing the Fermi surface of the separated and joined slabs clearly shows the new states appearing due to the T_d-T' interface, which is shown in Fig.13d for the case of the Spin-Orbit calculation. We have two pockets near 1 kT and 0.1 kT. When we plot the quantum oscillation frequencies as Gaussians with equal intensities, the agreement between experiment and calculation is quite impressive as shown in Fig.13d (bottom panel). Hence our slab-calculations directly show that the interface state is responsible for the high frequency quantum oscillations near 1 kT that we observed in the measurements, consistent with the presence of a TIN.

It is possible that folding back of the bands at the Fermi level due to the increased thickness of the $MoTe_2$ plane induces some new states, which might coincide with those new states in our finite slab calculation. In order to rule out this possibility, we examined the 2D contour plots of the Fermi surface of bulk T_d at 0.8 GPa with various $\mathbf{k}_z$ values as shown in Fig.14. We

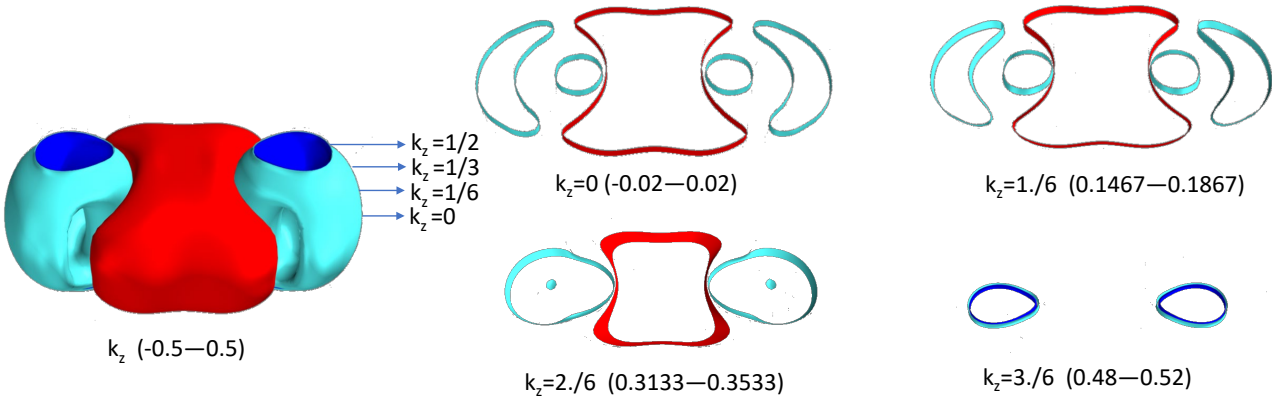

Supplementary Figure 14: **The 2D contours of 0.8 Gpa T_d-$MoTe_2$ Fermi surface at different $\mathbf{k}_z$ -value.** We tune $\mathbf{k}_z$ = n/6 with the some thickness ($\mathbf{k}_z$ -0.02, $\mathbf{k}_z$ +0.02), here n = 0, 1, 2 and 3. The maximum of extension of the Fermi surface in the $\mathbf{k}_x$ -$\mathbf{k}_y$ plane occurs when $\mathbf{k}_z$ = 0. While $\mathbf{k}_z$ = 1/3 (corresponding to the 3-layers case), the circular contour increases and can not go around the contour of the Fermi surface at $\mathbf{k}_z$ = 0, which conflicts with our interface calculations.

considered $\mathbf{k}_z$ = n/6 with some thickness ($\mathbf{k}_z$ -0.02, $\mathbf{k}_z$ + 0.02), here n = 0, 1, 2 and 3. The maximum of the extension of the Fermi surface in the $\mathbf{k}_x$ -$\mathbf{k}_y$ plane occurs at $\mathbf{k}_z$ = 0. Overall, contours for other values of $\mathbf{k}_z$ are smaller. In particular for $\mathbf{k}_z$ = 1/3 (associated with 3-layers case), the circular contour becomes larger but it is smaller than the one at $\mathbf{k}_z$ =0, conflicting with our interface calculations. Therefore, folding back of the Fermi surface bands with increased number of layers can not explain the additional orbits that we see in the joined-slab calculations.

H. Supplementary Note 7: Relation to Neutron Scattering Results

As a final note, we point out that we have performed very careful neutron diffraction measurements to characterise the crystal structure. Our neutron data already exclude all the hypothetical structures discussed here. However, it is important to show that even in the absence of neutron diffraction data, none of these potential structures can give rise to a quantum oscillations near 1 kT. Our supercell structure of T_d-T' as shown in Fig. 12 is also ruled out by the neutron diffraction measurements. Hence we do not have a superlattice formation with triple **c**-axis, and the calculated structure of T_d-T' shown in Fig. 12 should be considered as an approximate structure of the interface between two crystallites of T_d and T'phases. Our slab calculations clearly show that the interface of T_d-T' phase is needed to explain the observed high frequency oscillations. This is direct evidence of our picture of the TIN phase discussed in the main text.

I. Supplementary Note 8: Angle dependence of Shubnikov-de Haas oscillations at ambient pressure

Here we show angular magnetoresistance measured at ambient pressure and 1.8 K when magnetic field rotates from **c** axis to b axis as the insert figure in Fig. 15(a). The beat frequency increases with the increasing of θ, the angle between magnetic field and **c** axis as shown in Fig. 15(b). The cross section areas of two electron bands, F_α and F_β slightly increase with increasing of θ at 1.8 K.

In order to understand this weak angle dependence of the SdH oscillations, we have calculated the extremal orbits as the magnetic field is turned as in our measurements. The results are summarized in Figure 15(d). The calculated angle dependence is also very weak up to 40°. Due to spin-orbit splitting, near 40°-60°, the calculated orbit frequency is suddenly almost doubled with a resulting complicated orbit that involves both the cup surface and the interior of the mug-shape surface. After this sudden increase, a new orbit is obtained as the interior of the mug-shape surface (see Fig. 15(d) which has, interestingly almost the same magnitude as the original frequency. Hence, the overall angle dependence is very weak, as we found in our measurements. It is unlikely for the electrons to oscillate around such a complicated orbit coherently and therefore one may expect small intensity, which is consistent with decreasing intensity in our measurements.

The angle dependence of SdH oscillations at ambient pressure maps out two 3D topological Fermi surfaces of two electron pockets, analyzed using a multiband LK fitting in equation (11). From the magnetoresistance raw data at ambient pressure, we subtract the second order polynomial background. The FFT spectrum shows three bands, F_γ = 32.5 T, F_α = 240.5 T, F_β = 258.0 T and their second and third order harmonic oscillations. The higher harmonic peaks of F_α and F_β indicate high

quality and homogeneity of the measured sample. The 1.8 K SdH oscillation data were fitted to an equation describing multiple bands of a three dimensional LK formula, resulting in the corresponding Berry phases, ($\phi_\gamma = \pi$, $\phi_\alpha = 0.88\pi$, and $\phi_\beta = 0.88\pi$), indicating that T_d-$MoTe_2$ at ambient pressure is a possible three dimensional topological semimetal with 3D topological phase shift, $\delta = -\frac{1}{8}$[15,16] for electron pocket using equation (11).

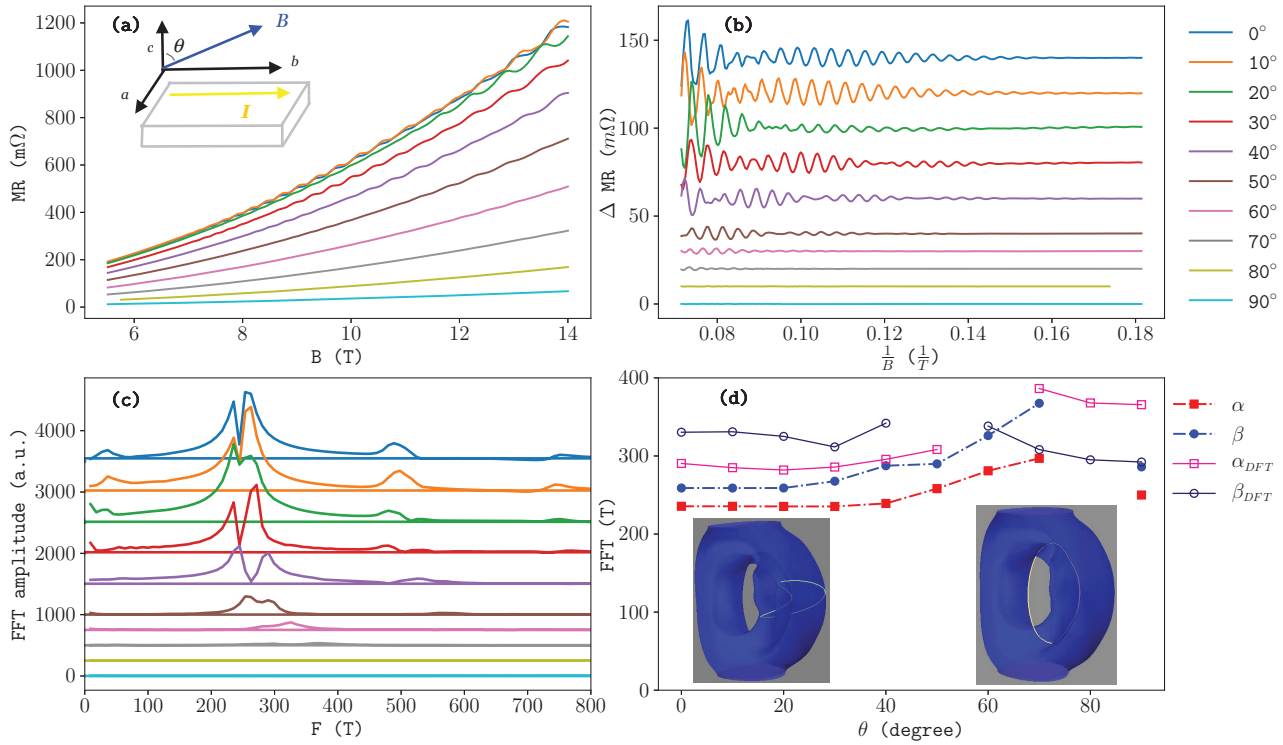

Supplementary Figure 15: **The angle dependent quantum oscillations of bulk $MoTe_2$ at 1.8 K and ambient pressure.** (a) The longitudinal MR measured when magnetic field moves from **c** axis to **b** axes (**B** // **c** axis, θ= 0). Schematic represents the four-point magnetoresistance measurement, in which current flows along the **b** axis, and magnetic field is rotated from the **c** axis to the **b** axis with angle θ. (b) The corresponding SdH oscillations were observed by calculating the oscillatory magnetoresistance $\Delta\rho = \rho - \rho_{\text{background}}$ above 5.5 T to 14 T. (c) The FFT spectrum of SdH oscillations as a function of the frequency shows three pockets, whose oscillation frequencies slightly increase above $\theta > 50°$. (d) The extracted angle-dependence of the oscillation frequencies along with DFT-calculations. The angle dependence of the quantum oscillations for the cup-shape orbit as the magnetic field is turned from **c**-axis (left) to **b**-axis (right). The insets show the Fermi surface and the corresponding orbits; For field direction near 40-60°, due to two closely related Fermi surfaces due to SO interactions and the complicated the mug-shape surface, the extremal orbit is rather complicated involving both the cup-portion of the surface and the interior of the mug-shape surface, which may explain the weak intensity of the oscillations for field directions near **b**-axis.

J. Supplementary Note 9: Analysis of Shubnikov-de Haas oscillations

The definitions of phase shift and Berry's phase are derived from the Lifshitz-Onsager quantization relation. By globally fitting the data to the Lifshitz-Kosevich formula using the program Bumps, we calculate uncertainty and correlation of the Dingle temperature and Berry's phase.

The general form of longitudinal conductivity is $\sigma_{xx} = \frac{\rho_{xx}}{(\rho_{xx}^2+\rho_{xy}^2)}$, here, ρ_{xx} and ρ_{xy} are the longitudinal and transverse resisitivity. In $MoTe_2$, the longitudinal resistivity is always much larger than transverse (Hall) resistivity ($\rho_{xx} >> \rho_{xy}$, three to four orders larger below 2 GPa[20]) and $\sigma_{xx} \approx \rho_{xx}^{-1}$.

The modified Lifshitz-Onsager quantization relation describes the closed trajectory of a charge carrier by an external magnetic field B as a function of Berry's phase and Zeeman splitting parameter S,

$$A_n \frac{\hbar}{eB} = 2\pi(n + \frac{1}{2} - \frac{\Phi_B}{2\pi} \pm \frac{1}{2}S) = 2\pi(n + \gamma \pm \frac{1}{2}S). \quad (2)$$

Here, A_n is the cross-sectional area of the Fermi surface related to the Landau level (LL) n, Berry phase Φ_B, and splitting parameter is defined as $S = \frac{1}{2} g \frac{m*}{m_0}$. $m*$ is the effective mass of the charge carrier and g is the Landau g factor.

To analyze the bulk SdH oscillations signal, we adopt the formula of ρ_{xx},

$$\rho_{xx} = \rho_0\{1 + \frac{5}{2}\sum_{r=1}^{\infty} b_r \cos(\theta \pm rS\pi) + R\}, \tag{3}$$

where

$$R = \frac{3}{8}\frac{\hbar\omega_c}{E_F}\{\sum_{r=1}^{\infty} b_r[\alpha_r \cos(\theta \pm rS\pi) + \beta_r \sin(\theta \pm rS\pi)] - ln(1 - e^{-\frac{4\pi\Gamma}{\hbar\omega_c}})\}, \tag{4}$$

$$b_r = \frac{1}{r^{\frac{1}{2}}}(\frac{\hbar\omega_c}{2E_F})^{\frac{1}{2}} \frac{2\pi^2 k_B T/\hbar\omega_c}{\sinh(2\pi^2 k_B T r/\hbar\omega_c)} e^{-\frac{2\pi\Gamma}{\hbar\omega_c} r}, \tag{5}$$

$$\alpha_r = 2r^{\frac{1}{2}} \sum_{s=1}^{\infty} \frac{1}{[s(r+1)]^{\frac{1}{2}}} e^{-\frac{4\pi\Gamma}{\hbar\omega_c} s}, \tag{6}$$

$$\beta_r = r^{\frac{1}{2}} \sum_{s=1}^{r-1} \frac{1}{[s(r-s)]^{\frac{1}{2}}}, \tag{7}$$

and

$$\theta = 2\pi(r(\frac{B_F}{B} + \gamma) - \delta). \tag{8}$$

Here, ρ_0 is the nonoscillatory component of resistivity at zero field, and other parameters are Dingle temperature $\mathrm{T_d}$, oscillatory frequency $\mathrm{B_F}$, cyclotron frequency $\omega_c = eB/m^*$, Boltzmann's constant k_B and harmonic order r. The Landau level-broadening width Γ is caused by scattering and associated with Dingle temperature $\Gamma = \pi k_B \mathrm{T_D}$. To extract the Zeeman splitting, we take the sum of the phase term as

$$\cos(\theta + rS\pi) + \cos(\theta - rS\pi) = 2\cos\theta\cos(Sr\pi) = 2\cos(2\pi(r(\frac{B_F}{B} + \gamma) - \delta))\cos(\frac{1}{2} r\pi g \frac{m*}{m_0})$$

$$\sin(\theta + rS\pi) + \sin(\theta - rS\pi) = 2\sin\theta\cos(Sr\pi) = 2\sin(2\pi(r(\frac{B_F}{B} + \gamma) - \delta))\cos(\frac{1}{2} r\pi g \frac{m*}{m_0})$$

Here, $2\cos(\frac{1}{2} r\pi g \frac{m*}{m_0})$ is a reduction factor due to the Zeeman splitting.

Experimentally, oscillatory frequency (B_F) and effective mass (m*) are determined through the FFT of the quantum oscillations signal and the temperature dependence of the amplitude of the oscillations, typically determined at an extremum. δ is the topological phase shift, which arises from the dimensionality of the Fermi surface, $\delta = 0$ (or $\delta = \pm\frac{1}{8}$) for a 2D (or 3D) system[15,16]. In 3D Weyl semimetals without lattice inversion symmetry, the topological phase shift could be either $\pm\frac{1}{8}$ or $\pm\frac{5}{8}$[18]. A nontrivial Berry's phase is defined as $|\gamma - \delta| = |1/2 - \phi_B/2\pi - \delta|$ between 0 and 1/8. Berry's phase determination is very sensitive to the Zeeman effect and the Fermi surface might distort close to the quantum limit. The coefficients of R (Eqn. 4) are very small for the quantum oscillation frequencies and magnetic fields relevant to our measurements and do not affect our analysis.

Therefore, the longitudinal resistivity is

$$\rho_{xx} = \rho_0\{1 + 5\sum_{r=1}^{\infty}[(\frac{\hbar\omega_c}{E_F})^{1/2}\cos(\frac{r\pi g m*}{2m_0}) e^{\frac{-2\pi^2 k_B T_D r}{\hbar\omega_c}} \frac{\frac{2\pi^2 k_B T r}{\hbar\omega_c}}{\sinh(\frac{2\pi^2 k_B T r}{\hbar\omega_c})} \cos(2\pi((\frac{B_F}{B} + \gamma)r - \delta))\}. \tag{9}$$

These periodic SdH oscillations in magnetroresistance follow the Lifshitz-Kosevich (LK) formula for three-dimensional systems[17] as,

$$A(B,T) = \frac{\Delta\rho}{\rho_0} \propto (\frac{\hbar\omega_c}{E_F})^{1/2} \exp(-2\pi^2 k_B T_D/\hbar\omega_c) \frac{2\pi^2 k_B T/\hbar\omega_c}{\sinh(2\pi^2 k_B T/\hbar\omega_c)}. \tag{10}$$

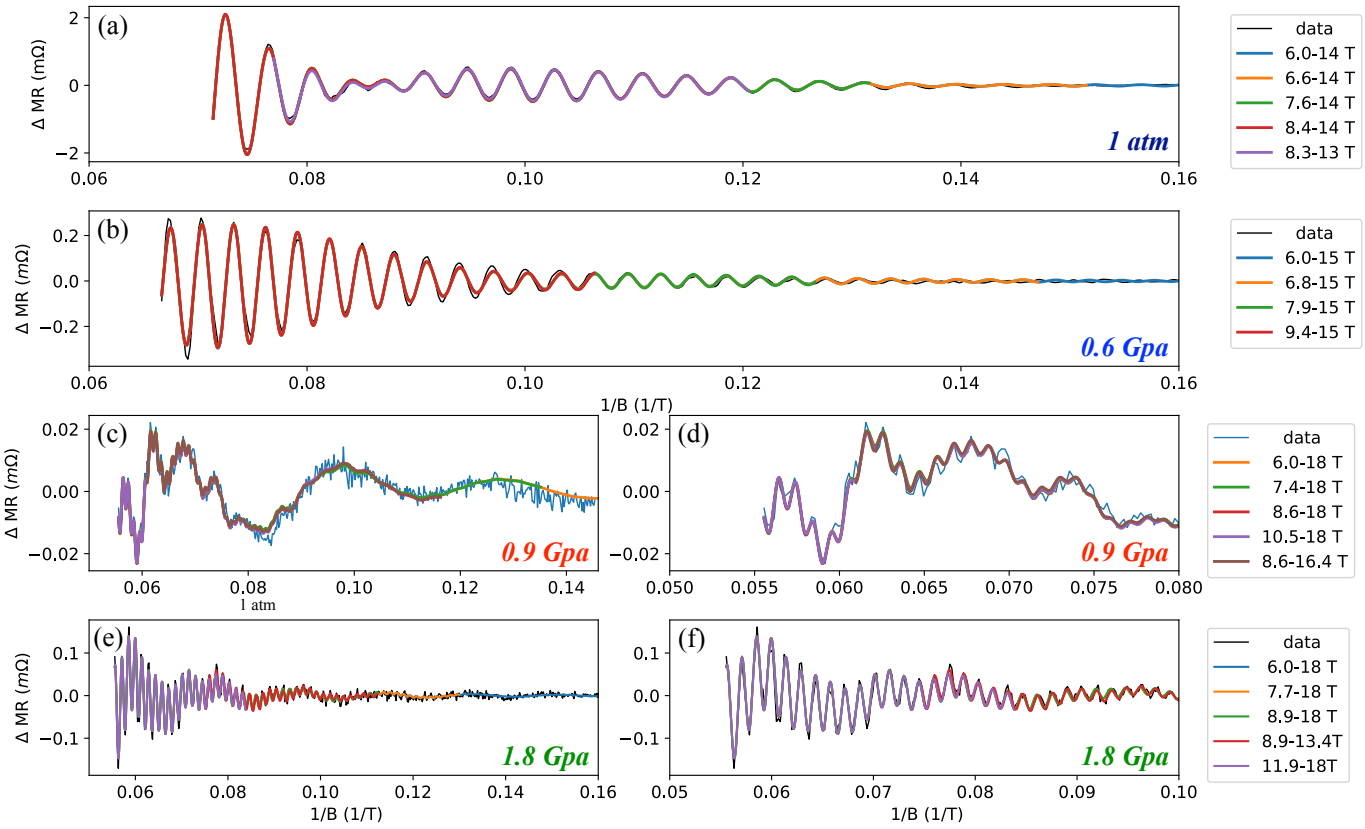

Supplementary Figure 16: **The fit of the oscillation patterns.** Multiple band LK fits to $MoTe_2$ quantum oscillations measured at 1.8 K and (a) 1 atm (Physical Property Measurement System PPMS), (b) 0.6 GPa (dilution refrigerator down to 0.1 K). Higher pressure cases (c, d) 0.9 GPa at 0.27 K and (e,f) 1.8 GPa at 0.3 K (Oxford Heliox).

The first order harmonic of the 3D LK formula dominates the oscillation signal[17], giving

$$\rho_{xx} = \rho_0[1 + A(B,T)\cos(\frac{\pi g m*}{2m_0})\cos 2\pi(\frac{B_F}{B} - \delta + \gamma)]. \tag{11}$$

If the Zeeman splitting term does not change within the experimental magnetic field (namely, each g factor for each band remains a constant over the experimental field range), this term is decoupled from the phase of oscillations, such that

$$\rho_0 A(B,T)\cos(\frac{\pi g m*}{2m_0}) = A_0, \tag{12}$$

Thus, the g factor only modifies the oscillation amplitude (A_0) and will not change the phase of oscillations. Therefore, the Berry's phase and the phase shift δ are decoupled from the g factor and Zeeman parameter. Following convention, the amplitude A is kept positive. Typically, the g factor of these transition metal dichalcogenide are positive. Note that when 4n+1 < $\frac{gm*}{m_0}$ < 4n + 3, where n is an integer, Eq. 12 yields a negative value of A_0. This condition is met in the conventional case when g = 2 and $\frac{m*}{m_0}$ = 1. In our fits, this results in a π phase shift, which is captured by the $\frac{1}{2}$ term in the equation $\frac{1}{2}$ - $\frac{\phi_B}{2\pi}$ - δ. We expect that this condition is true also in our analysis. The values of ϕ_B displayed in Supplementary Tables 5 and Supplementary Table 6 correspond to the measured phase shift, with a factor of $\frac{1}{2}\times(2\pi)$ subtracted. An important caveat is that the value of g is not independently known, and it is therefore not known whether the extra factor of $\frac{1}{2}\times(2\pi)$ is always appropriate. However, due to the large variation in m* (Supplementary Table 6), it would require a dramatic coincidence for every band to exhibit a value of $\frac{gm*}{m_0}$ that results in a positive amplitude. We demonstrate the LK fits under different field ranges for four pressure cases as shown in figure 16. The consistent π Berry's phases in Table 6 confirm that the g factor for each band is a constant and decoupled from Berry's phase.

P (GPa)	field range (T)	ϕ_γ (π)	ϕ_α (π)	ϕ_β (π)	
$\sim$0	6-14	0.97	0.89	0.88	
	6.6-14	0.999	0.883	0.883	
	7.6-14	1.000	0.877	0.879	
	8.4-14	1.000	0.871	0.873	
	8.4-13	0.947	0.876	0.877	
0.6	6-15	0.95	0.89	0.88	
	6.8-15	0.964	0.878	0.886	
	7.9-15	0.963	0.878	0.889	
	9.4-15	0.963	0.877	0.894	
P (GPa)	field range (T)	ϕ_λ (π)	ϕ_μ (π)	ϕ_ν (π)	ϕ_δ (π)
0.9	6.8-18	0.86	0.93	0.88	1.02
	7.4-18	0.862	0.932	0.881	1.008
	8.6-18	0.861	0.932	0.881	1.009
	10.5-18	0.862	0.934	0.882	1.009
	8.6-16.4	0.867	0.946	0.885	1.038
P (GPa)	field range (T)	ϕ_ω (π)	ϕ_σ (π)	ϕ_ζ (π)	ϕ_η (π)
1.8	6-18	0.98	0.77	1.20	1.10
	7.7-18	0.966	0.756	1.188	1.111
	8.88-18	0.963	0.759	1.187	1.112
	8.9-13.4	0.935	0.776	1.290	1.052
	11.93-18	0.961	0.758	1.182	1.113

Supplementary Table 5: **Berry's phase determined over different field ranges.** Here, we show that the consistent Berry's phase is consistent for fits performed over different field ranges. The invariant of π Berry's phase suggests that g factor does not change within the field range.

K. Supplementary Note 10: Global fitting- Bumps

Finding the global minimum of fits to the Lifshitz-Kosevich formulam with multiple bands is nontrivial because of the large number of fitting parameters, which may be correlated. Bumps is a set of free and public routines for complicated curve fitting, uncertainty analysis and correlation analysis from a Bayesian perspective[19]. Bumps provides uncertainty analysis and explores all viable minima and finds confidence intervals on the parameters based on uncertainty from experimental errors. First, we applied gradient descent to quickly search local minimum and included the real experimental errors for global fitting of the LK formula, in other words, to the full magnetic field range of measured quantum oscillations. To see the distributions of uncertainty and correlation plots, we ran Bumps for the the rest of the variables: amplitude, Dingle temperature and Berry phase, and found convergence of these fitting parameters.

Bumps includes Markov chain Monte Carlo (MCMC) methods[19] to compute the joint distribution of parameter probabilities. The MCMC explores parameter space using a random walk and requires hundreds of thousands of function evolutions to explore the search space. The histogram range represents the 95 $\%$ credible interval, and the shaded region represents the 68 $\%$ credible interval. For full uncertainty analysis, Bumps uses a random walk to explore the viable parameter space near the minimum, showing pair-wise correlations between the different parameter values. The 2D correlation plots indicate the correlation relationship between multiple parameters in the fitting function. We checked the convergence of fits and compared different local minima to get the global minimum. Figure 16 shows the best fit curves of SdH oscillation signal from 1 atm to 1.8 GPa. We show the expectation value and uncertainties for fitting data at 1 atm (Fig. 17), 0.6 GPa (Fig. 18), 0.9 GPa (Fig. 19) and 1.8 GPa (Fig. 20).

P (GPa)	label	F (T)	T_d (K)	m^* (m_e)	ϕ (π)	μ(cm^2/v$_S$)
∼0	γ	32.50	19.81	0.31	0.97	348.30
	α	240.50	4.99	0.53	0.89	809.90
	β	258.00	6.14	0.59	0.88	557.77
0.6	γ	35.00	18.20	0.30	0.95	456.46
	α	330.30	4.16	0.71	0.89	720.95
	β	355.00	9.16	0.63	0.88	372.41
0.9	λ	32.00	7,91	0.21	0.87	1635.88
	μ	170.00	5.12	1.02	0.93	436.44
	ν	245.00	2.97	1.08	0.88	629.26
	δ	966.00	3.54	1.75	1.02	350.83
1.8	ω	53.00	3.48	0.47	0.98	1324.20
	σ	110.00	8.48	0.57	0.77	438.90
	ζ	158.00	6.88	0.81	1.20	381.37
	η	690.00	3.94	0.97	1.10	558.02

Supplementary Table 6: **The fitting parameters of the LK formula fits to $MoTe_2$ quantum oscillations under pressure P.** We obtained oscillation frequency F from FFT, effective mass m^* and corresponding quantum mobility μ from the temperature dependence of FFT. Here, the sum of Berry's phase and phase shift, ϕ (ϕ = $\frac{1}{\pi}\phi_B \pm \delta$ and phase shift determined by the dimensionality of Fermi surface, $\delta = 0$ or $\delta = \pm\frac{1}{8}$ for 2D or 3D) could be directly determined from the LK formula.

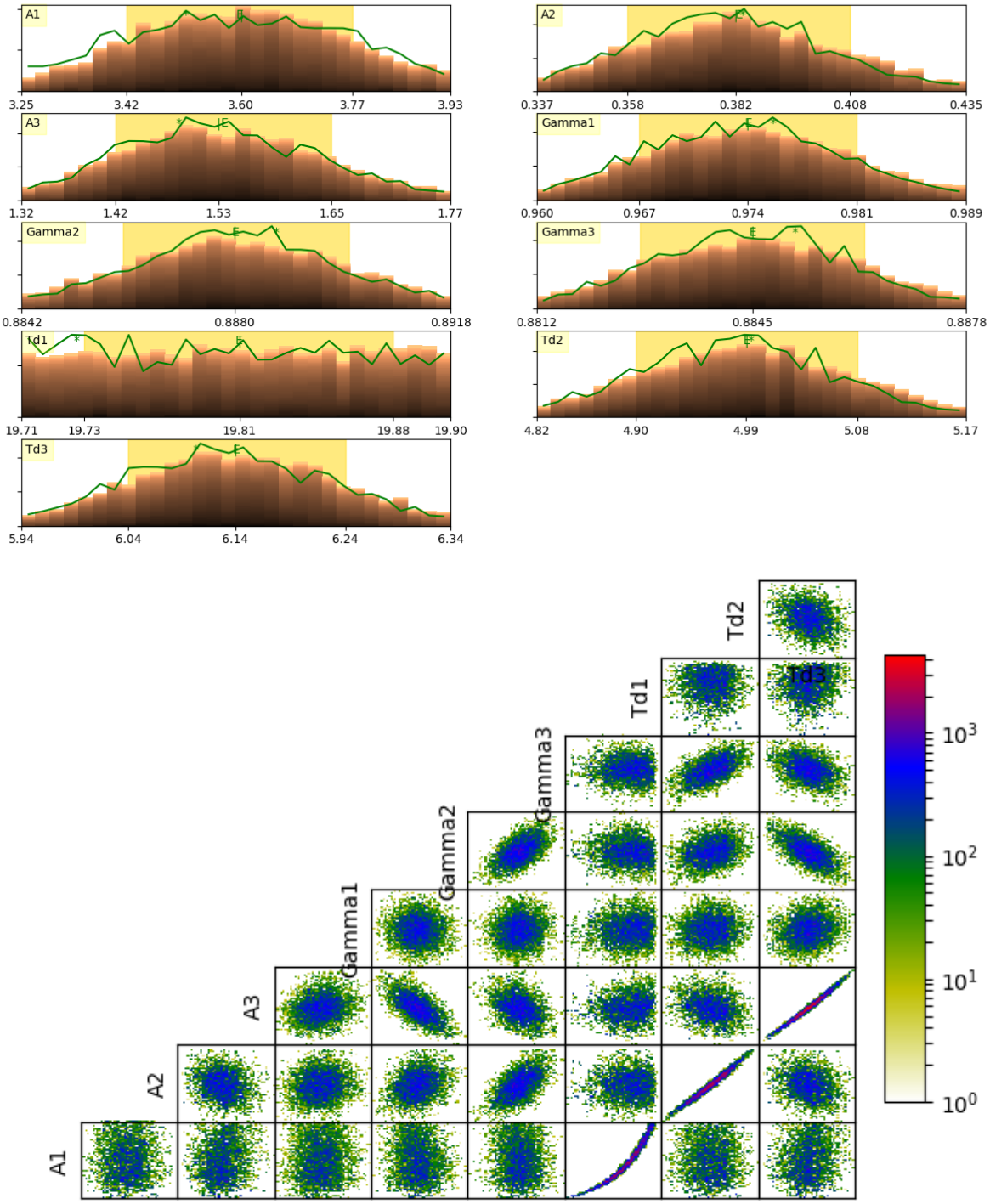

Supplementary Figure 17: **The uncertainty and correlation plot of fitting parameters in LK formula at ambient pressure.** This is the (a) uncertainty of Lifshitz-Kosevich formula fitting to $MoTe_2$ data at 1.8 K and 1 atm. The Berry's phases of the γ(Gamma1), α(Gamma2), and β(Gamma3) oscillations are $(0.97 \pm 0.02)\pi$, $(0.89 \pm 0.01)\pi$ and $(0.88 \pm 0.01)\pi$. (b) The 2D correlation plots between each pair of parameters in the fits. There is positive correlation between maximum oscillation amplitude and Dingle temperature. The Berry's phase shows no correlation with Dingle temperature and oscillation amplitude.

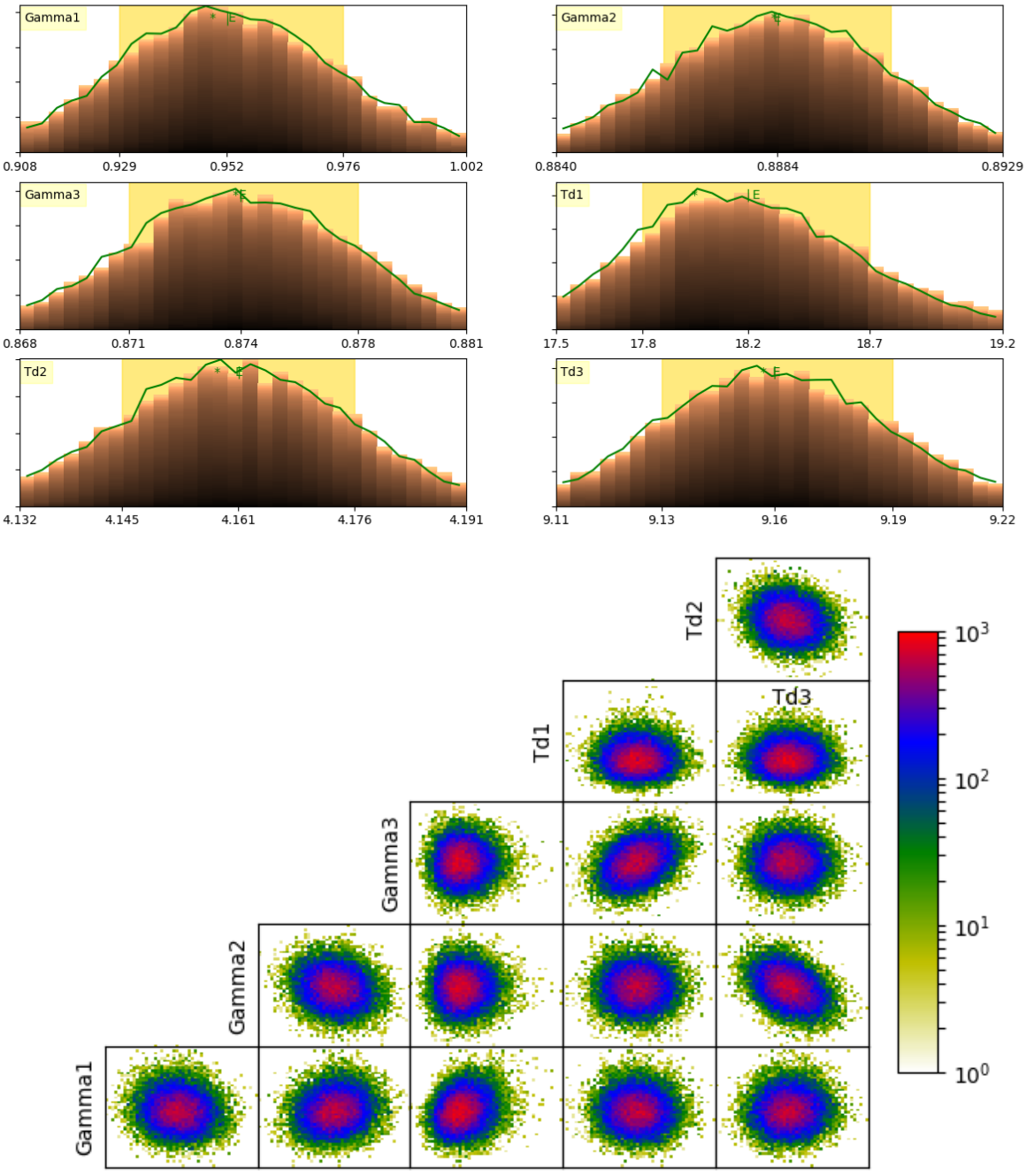

Supplementary Figure 18: **The uncertainty and correlation plot of fitting parameters in LK formula at 0.6 GPa.** This is the (a) uncertainty of Lifshitz-Kosevich formula fitting to $MoTe_2$ data at 0.1 K and 0.6 GPa. The Berry's phases of the γ(Gamma1), α(Gamma2), and β(Gamma3) oscillations are $(0.95 \pm 0.05)\pi$, $(0.89 \pm 0.01)\pi$ and $(0.87 \pm 0.01)\pi$. (b) The 2D correlation plots between each pair of parameters in the fits. The Berry's phase shows no correlation with Dingle temperature.

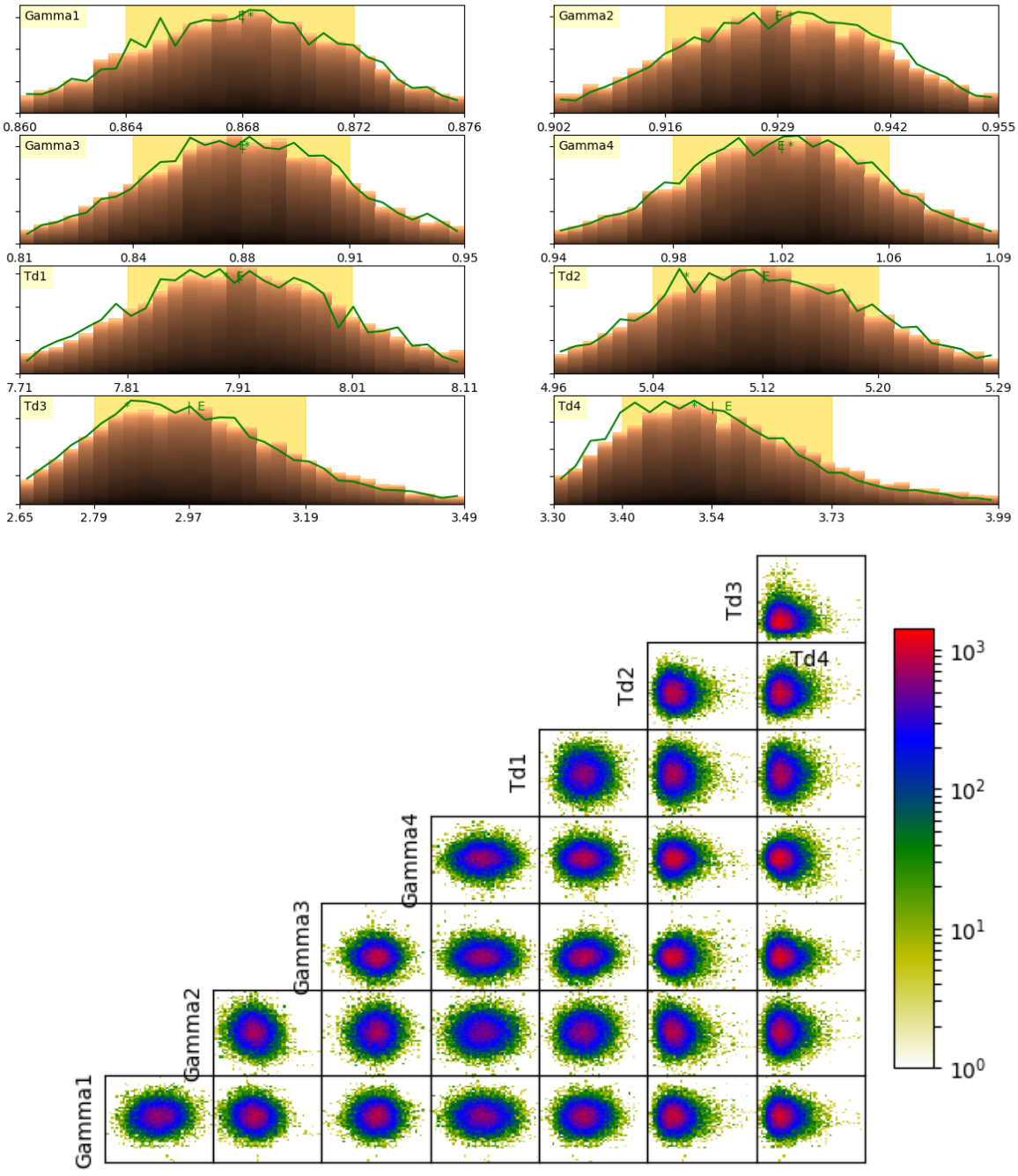

Supplementary Figure 19: **The uncertainty and correlation plot of fitting parameters in LK formula at 0.9 GPa.** This is the (a) uncertainty of Lifshitz-Kosevich formula fitting to $MoTe_2$ data at 0.27 K and 0.9 GPa. The Berry's phase of the λ(Gamma1), μ(Gamma2), ν(Gamma3), and δ(Gamma4) oscillations are $(0.87 \pm 0.01)\pi$, $(0.93 \pm 0.02)\pi$, $(0.88 \pm 0.07)\pi$, and $(1.02 \pm 0.08)\pi$. (b) The 2D correlation plots between each pair of parameters in the fits. The Berry's phase shows no correlation with Dingle temperature.

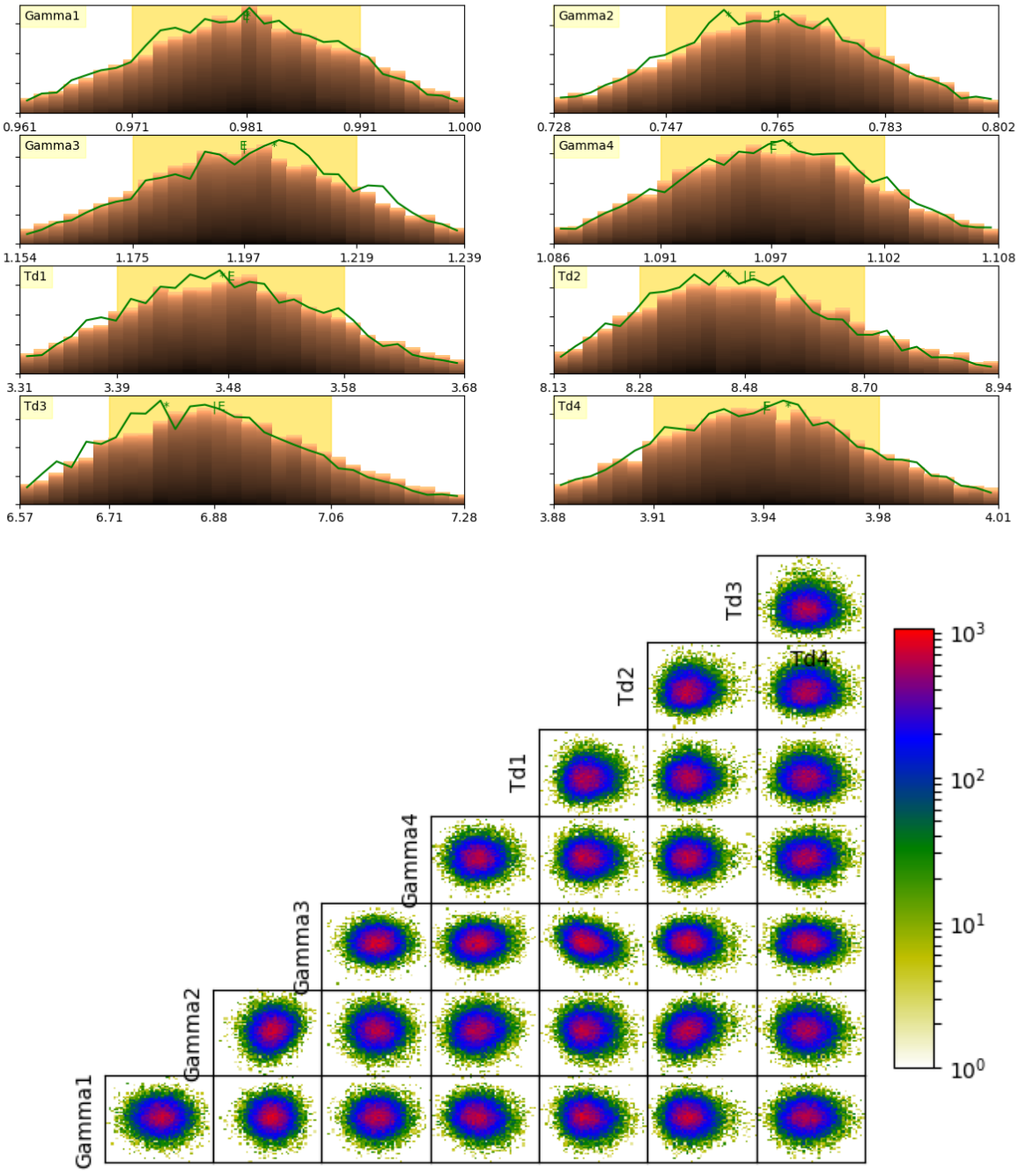

Supplementary Figure 20: **The uncertainty and correlation plot of fitting parameters in LK formula at 1.8 GPa.** This is the (a) uncertainty of Lifshitz-Kosevich formula fitting to $MoTe_2$ data at 0.3 K and 1.8 GPa. The Berry's phase of the ω(Gamma1), σ(Gamma2), ζ(Gamma3), and η(Gamma4) oscillations are $(0.98 \pm 0.02)\pi$, $(0.77 \pm 0.03)\pi$, $(1.20 \pm 0.03)\pi$, and $(1.10 \pm 0.01)\pi$. (b) The 2D correlation plots between each pair of parameters in the fits. The Berry's phase shows no correlation with Dingle temperature.

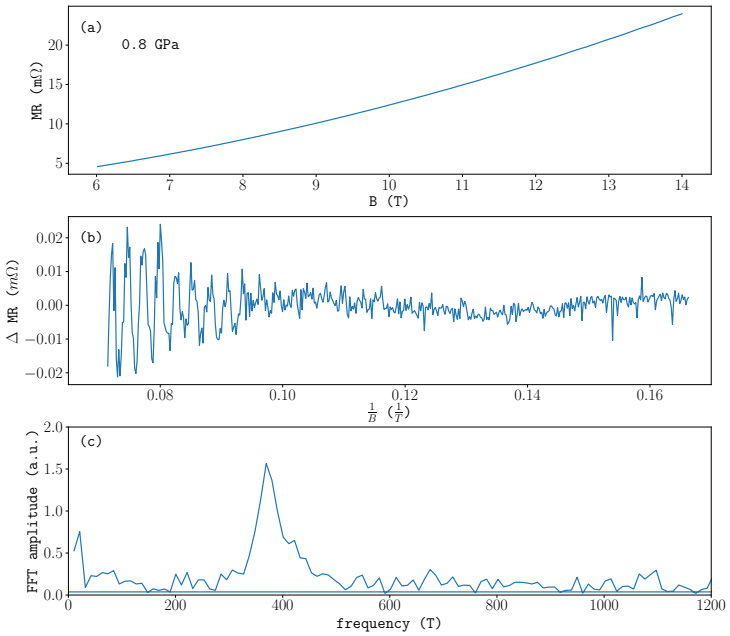

Supplementary Figure 21: **Quantum oscillations of magnetoresistance in $MoTe_2$ at 0.8 GPa.** (a) The longitudinal MR, (b) SdH oscillations and (c) corresponding FFT of the bulk $MoTe_2$ sample measured at 1.8 K with magnetic field parallel to **c** axis.

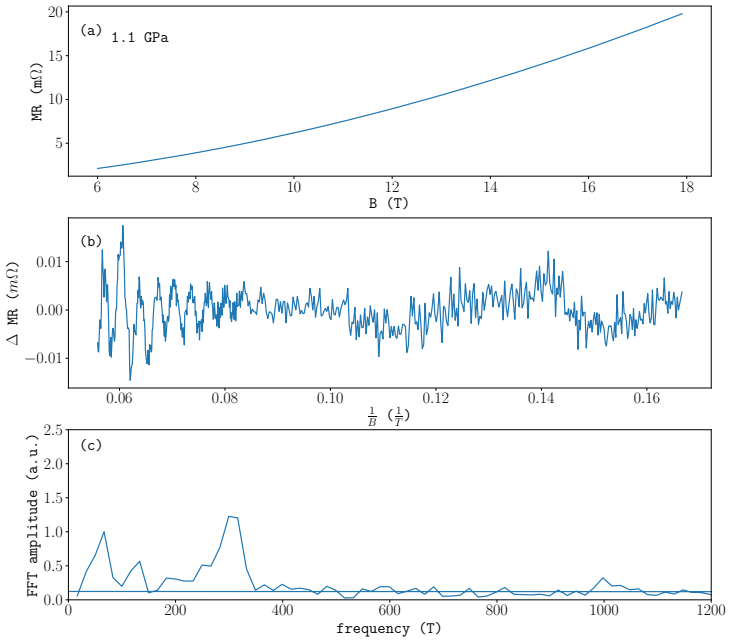

Supplementary Figure 22: **Quantum oscillations of magnetoresistance in $MoTe_2$ at 1.1 GPa.** (a) The longitudinal MR, (b) SdH oscillations and (c) corresponding FFT of the bulk $MoTe_2$ sample measured at 0.3 K with magnetic field parallel to **c** axis.

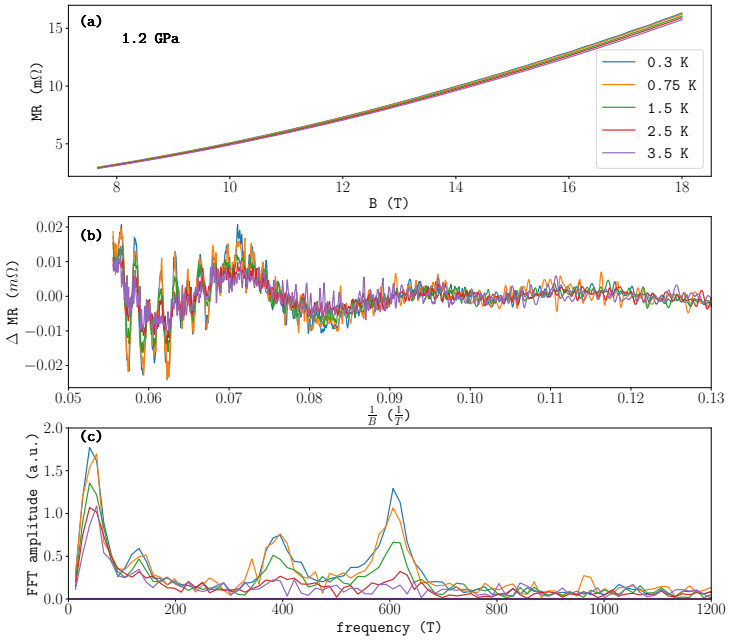

Supplementary Figure 23: **Quantum oscillations of magnetoresistance in $MoTe_2$ at 1.2 GPa.** (a) The longitudinal MR, (b) SdH oscillations and (c) corresponding FFT of the bulk $MoTe_2$ sample measured with magnetic field parallel to **c** axis.

[1] Colin Heikes et al. Mechanical control of crystal symmetry and superconductivity in Weyl semimetal $MoTe_2$. *Phys. Rev. M*. **2**, 074202 (2018).

[2] Weida Wu et al. Magnetic imaging of a supercooling glass transition in a weakly disordered ferromagnet. *Nature Materials*. **5**, 881-886 (2006).

[3] S. B. Roy et al. Evidence of a magnetic glass state in the magnetocaloric material Gd_5Ge_4. *Phys. Rev. B.* **74**, 012403 (2006).

[4] Junjie Yang et al. Elastic and electronic tuning of magnetoresistance in $MoTe_2$. *Science Advances*. **3**, 12 (2017).

[5] P. Giannozzi, et al. Quantum espresso: a modular and open-source software project for quantum simulations of materials. *J. Phys.: Condens. Matter* **21**, 395502 (2009).

[6] P. E. Blöchl Projector augmented-wave method. Phys. Rev. B **50**, 17953-17979 (1994).

[7] G. Kresse and D. Joubert From ultrasoft pseudopotentials to the projector augmented-wave method. *Phys. Rev. B* **59**, 1758 (1999).

[8] J. P. Perdew, K. Burke, and M. Ernzerhof Generalized gradient approximation made simple. *Phys. Rev. Lett.* **77**, 3865-3868 (1996).

[9] S. Grimme Semiempirical GGA-type density functional constructed with a long-range dispersion correction. *J. Comp. Chem.* **27**, 1787-1799 (2006).

[10] N. Xu et al. Evidence of Coulomb-interaction-induced Lifshitz transition and robust hybrid Weyl semimetal in T_d-$MoTe_2$. *Phys. Rev. Lett.* **121**, 136401 (2018).

[11] N. Aryal and E. Manousakis Importance of electron correlations in understanding the photo-electron spectroscopy and the Weyl character of $MoTe_2$. *Phys. Rev. B* **99**, 035123 (2019).

[12] Zhijun Wang et al. Higher-order topology, monopole nodal lines, and the origin of large Fermi arcs in transition metal dichalcogenides XTe_2 (X = Mo, W). *Phys. Rev. Lett.* **123**, 186401 (2019).

[13] Ramachandran, P. and Varoquaux, G. Mayavi: 3d visualization of scientific data. *IEEE Computing in Science & Engineering*, **13** (2), 40-51 (2011).

[14] P.M.C. Rourke and S.R. Julian Numerical extraction of de Haas-van Alphen frequencies from calculated band energies. *Comp. Phys. Commun.* **183**, 324-332 (2012).

[15] Igor A. Luk′yanchuk, and Yakov Kopelevich Phase analysis of quantum oscillations in graphite. *Phys. Rev. Lett* **93**, 166402 (2004).

[16] Igor A. Luk′yanchuk, and Y Kopelevich Dirac and normal Fermions in graphite and graphene: implications of the quantum Hall effect. *Phys. Rev. Lett* **97**, 256801 (2006).

[17] H. Murakawa et al. Detection of Berry's phase in a bulk Rashba semiconductor. *Science* **342**, 1490-1493 (2013).

[18] C.M. Wang, Hai-Zhou Lu, and Shun-Qing Shen Anomalous phase shift of quantum oscillations in 3D topological semimetals. *Phys. Rev. Lett* **117**, 077201 (2016).

[19] P. A. Kienzle, J. Krycka, N. Patel and I. Sahin, Bumps (Version 0.7.5.4) *University of Maryland, College Park, MD*, (2011)

[20] Sangyun Lee et al. Origin of extremely large magnetoresistance in the candidate type-II Weyl semimetal $MoTe_{2-x}$. *Scientific Reports* **8**, 13939 (2018)